PREFERRED ORIENTATIONS AND ANISOTROPY IN SHALES: CALLOVO-OXFORDIAN SHALE (FRANCE) AND OPALINUS CLAY (SWITZERLAND)

H.-R. WENK[1], M. VOLTOLINI[1], M. MAZUREK[2], L. R. VAN LOON[3], AND A. VINSOT[4]

[1] Department of Earth and Planetary Science, University of California, Berkeley CA 94720, USA
[2] Institute of Geological Sciences, University of Bern, Switzerland
[3] Paul Scherrer Institut, Villigen, Switzerland
[4] Andra, Laboratoire souterrain de Meuse/Haute-Marne, Bure, France

Abstract—Anisotropy in clay-rich sedimentary rocks is receiving increasing attention. Seismic anisotropy is essential in the prospecting for petroleum deposits. Anisotropy of diffusion has become relevant for environmental contaminants, including nuclear waste. In both cases, the orientation of component minerals is a critical ingredient and, largely because of small grain size and poor crystallinity, the orientation distribution of clay minerals has been difficult to quantify. A method is demonstrated that relies on hard synchrotron X-rays to obtain diffraction images of shales and applies the crystallographic Rietveld method to deconvolute the images and extract quantitative information about phase fractions and preferred orientation that can then be used to model macroscopic physical properties. The method is applied to shales from European studies which investigate the suitability of shales as potential nuclear waste repositories (Meuse/Haute-Marne Underground Research Laboratory near Bure, France, and Benken borehole and Mont Terri Rock Laboratory, Switzerland). A Callovo-Oxfordian shale from Meuse/Haute-Marne shows a relatively weak alignment of clay minerals and a random distribution for calcite. Opalinus shales from Benken and Mont Terri show strong alignment of illite-smectite, kaolinite, chlorite, and calcite. This intrinsic contribution to anisotropy is consistent with macroscopic physical properties where anisotropy is caused both by the orientation distribution of crystallites and high-aspect-ratio pores. Polycrystal elastic properties are obtained by averaging single crystal properties over the orientation distribution and polyphase properties by averaging over all phases. From elastic properties we obtain anisotropies for p waves ranging from 7 to 22%.

Key Words—Anisotropy, Illite, Kaolinite, Preferred Orientation, Rietveld Method, Shale.

INTRODUCTION

Argillaceous rocks such as clays and shales are being investigated as possible repositories for radioactive waste disposal because of their very low permeability and ability to retain radionuclides. These two characteristics are essential to keep the radionuclides, released during long-term storage, from entering the biosphere. For our study, we used sample materials and ancillary data from study sites in France and Switzerland. One site is located in the eastern part of the Paris basin (France). Here, the Meuse/Haute-Marne Underground Research Laboratory (MHM-URL, Bure) has been built to study a 130 m thick, flat-lying clayey formation of Callovo-Oxfordian age (150−160 My), 420−550 m below the surface (Andra, 2005a; Delay *et al.*, 2007). A drillhole, in which Opalinus Clay (middle Jurassic, 174 My) was investigated, is located near Benken, northeast of Zurich (Switzerland). Here, the formation is flat lying, undeformed, and occurs at a depth of 550−650 m below the surface (Nagra, 2002). Another study site in the Opalinus

Clay is the Mont Terri rock laboratory (Canton Jura, Switzerland), which is operated by an international consortium including several organizations dealing with radioactive waste disposal. This site, in contrast to the others, is not considered a potential disposal site but serves the purpose of developing *in situ* investigation techniques in an international framework. Here, the Opalinus Clay is located at a depth of ~270 m below the surface. The underground laboratory consists of a dedicated tunnel section which branches off an existing highway tunnel across the Mont Terri anticline in the Jura mountains (Pearson *et al.*, 2003; Thury and Bossart, 1999; Bossart and Thury, 2007). Folding of this thin-skinned mountain belt occurred between 10.5 and 3 My.

Shales display anisotropy of macroscopic elastic properties and this has long been a topic of interest (Crampin, 1981; Hornby, 1998; Hornby *et al.*, 1994; Sayers, 1994, 2005) and is investigated in particular with respect to seismic prospecting (Banik, 1984; Jones and Wang, 1981). The anisotropy of acoustic wave propagation has been measured in the laboratory under a variety of conditions (Johnston and Christensen, 1995; Vernik and Liu, 1997; Vernik and Nur, 1992; Wang, 2002). Several factors contribute to anisotropy of acoustic-wave propagation. The distribution of low-aspect-ratio pores

and the orientation distribution of minerals are most important.

In this study we explore the orientation of mineral components in shales with new diffraction methods that allow us to characterize the orientation distribution (OD) or texture quantitatively. Note that in this work we use the term "texture" as a synonym for crystallographic preferred orientation, rather than microstructure, as is universally accepted in materials science. The method, originally developed to investigate deformation effects in high-pressure, diamond anvil cell experiments (Wenk *et al.*, 2004), uses hard synchrotron X-rays and analysis of diffraction images. It has previously been applied to some relatively simple shales (Wenk *et al.*, 2007; Lonardelli *et al.*, 2007). Here we use it for the first time to study very complex materials with many phases, in order to characterize the texture for shale samples from MHM-URL (Bure), Benken, and Mont Terri. The ODs of the various samples are compared and discussed in the context of the stratigraphic-tectonic history. The contribution of preferred orientation to the anisotropy of elastic properties of the polycrystalline shale can be assessed by averaging single-crystal properties over the OD.

MATERIALS AND PETROGRAPHIC CHARACTERIZATION

Table 1 gives an overview of samples used for this study. At the Bure (MHM-URL) site, the Callovo-Oxfordian formation contains 25 to 55 wt.% clay minerals, associated with $23-42\%$ carbonates (calcite $\pm$ dolomite, ankerite), $20-31\%$ quartz and feldspars, and a small percentage of subordinate minerals (Andra, 2005a) (Figure 1a). Vertically, the formation is divided into three sedimentary sequences, the boundaries of which are outlined by thin carbonate deposits which can be correlated over large distances. The lower sequence is siltier than average, the central one is clay-rich and the upper sequence has the largest carbonate contents. These sequences express low cyclic variation in relative sea-level at the time of deposition (transgressive-regressive cycles, each lasting 2 to 3 My) (Andra, 2005b). Clay minerals include illite, an illite-smectite mixed-layer phase and subordinate kaolinite and chlorite. In the upper half of the profile, until ~490 m, the illite-smectite mixed-layer phase contains $50-70\%$ smectite and is disordered (R0 type). Below that depth, the mixed-layer phase is ordered (R1 type) and contains $20-40\%$ smectite layers. Kaolinite is more abundant in the lower part. The marked change in clay mineralogy is located within the central, clay-rich sequence. The vertical variability of clay mineralogy is due to primary deposition and not to different degrees of diagenetic overprint. The two samples used in this study are drill cores retrieved from the central, clay-rich sequence, one from the zone where the disordered illite-smectite phase dominates, one from the zone containing the ordered phase. The average clay-

Table 1. Sample locations.

| Formation	Sample ID	Locality	Depth (m)	Description
Callovo-Oxfordian shale	MHM-URL1 EST25680	MHM-URL, Bure, France	477.4	Black bioclastic and pyritic silty-calcareous shale
Callovo-Oxfordian shale	MHM-URL2 EST25376	MHM-URL, Bure, France	503.5	Black bioclastic and pyritic silty-calcareous shale
Opalinus Clay	Benken 1 MW44 12 06 02 PA3	Benken, Switzerland	563.75	Silty argillaceous marl
Opalinus Clay	Benken 2 MW44B 06 06 02	Benken, Switzerland	589.49	Sandy argillaceous marl
Opalinus Clay	Benken 3 4404 Dif OPA 1001 3B	Benken, Switzerland	636.74	Silty, calcareous shale
Opalinus Clay	Benken 4 MW44 30 04 02 2C	Benken, Switzerland	651.11	Calcareous shale
Opalinus Clay	Mont Terri 1	Mont Terri, Switzerland		Silty, calcareous shale, adjacent to a brittle fault
Opalinus Clay	Mont Terri 2	Mont Terri, Switzerland		Silty, calcareous shale from a brittle fault
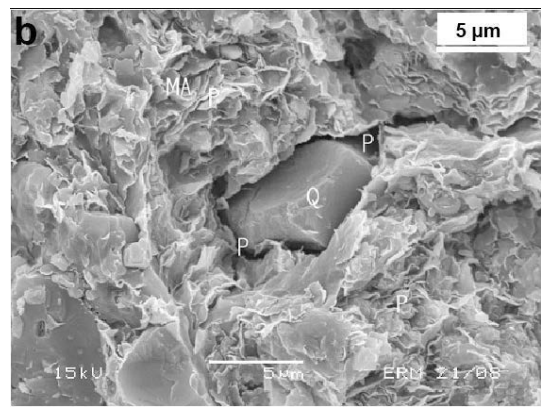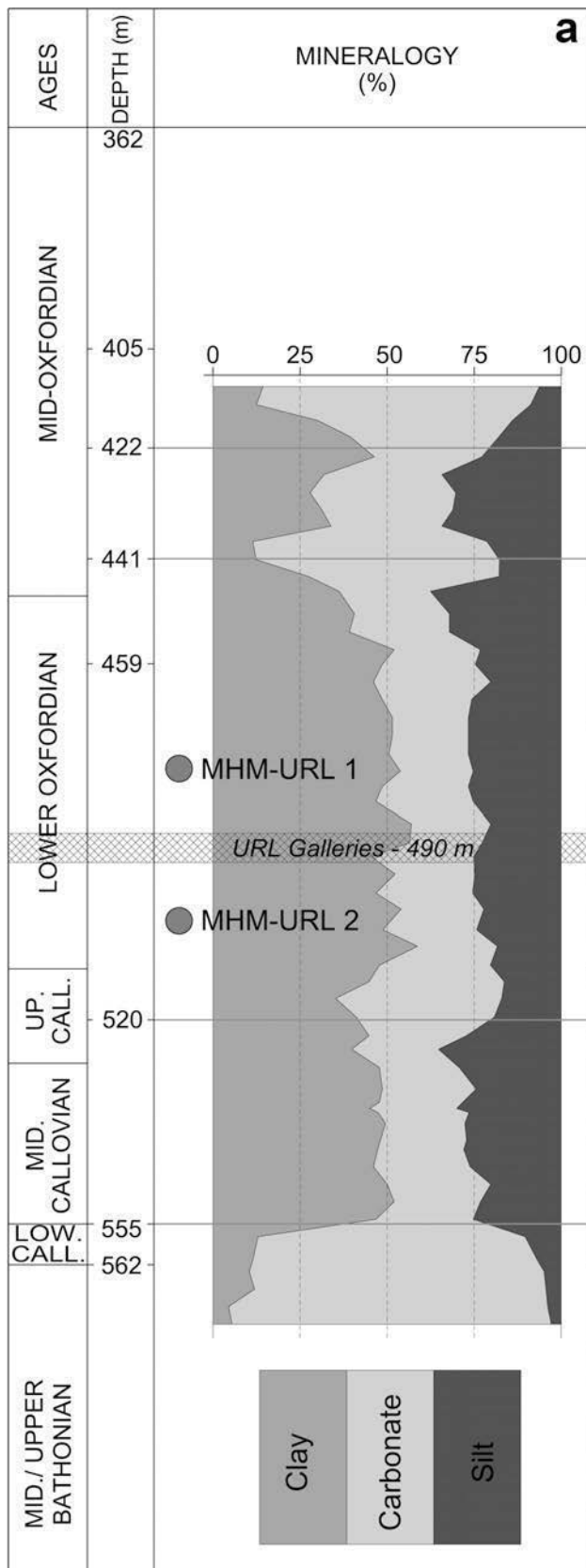
Figure 1. (a) Mineralogy of the Callovo-Oxfordian formation on the Meuse/Haute-Marne URL site (after Rebours *et al.*, 2007). (b) SEM image of typical microstructure with clay matrix (M), quartz grains (Q), and porosity (P) (modified from Sammartino *et al.*, 2001).

mineral contents in this depth region are ~50−55% (Figure 1a). Mineralogical transformations after deposition are processes of regional extent and mainly involve a limited carbonate cementation.

On the geological time scale, these changes occur at an early stage, before 100 My. The moderate thermal evolution, related to a moderate burial (<800 m) of the layer throughout its history, was not enough to initiate diagenetic transformation of clay phases (Andra, 2005b), but there are mineralogical transitions related to sedimentology (Claret *et al.*, 2004; Pellenard *et al.*, 1999). Petrophysical properties have been studied at various scales; they are tightly linked to the mineral content (Sammartino *et al.*, 2002, 2003; Gaucher *et al.*, 2004; Pellenard and Deconinck, 2006; Trouiller, 2006; Yven *et al.*, 2006; Homand *et al.*, 2006; Esteban *et al.*, 2007). The average water-accessible porosity is 18% (Andra, 2005a). The two samples used in this study are drill cores retrieved near the 490 m tunnel. The scanning electron micrograph (Figure 1b) displays a clay matrix with a wide dispersion of platelet orientations, large quartz fragments, and pores.

The Opalinus Clay is a formation with only limited heterogeneity on the scales of meters and more (Gautschi, 2001). On the centimeter scale, silty, quartz-rich lenses and diagenetic siderite concretions constitute conspicuous heterogeneities. On smaller scales, calcite bioclasts and disseminated silt layers are embedded in the clay-rich matrix (Figure 2, center and right). Alignment of clay minerals along the bedding plane is conspicuous. With the exception of quartz-rich, silty lenses, the Opalinus Clay is not cemented. The mineralogical composition of the Opalinus Clay includes 40−70 wt.% clay minerals, 10−30 wt.% carbonates (mainly calcite, subordinate siderite, and ankerite), 10−30 wt.% quartz and accessory feldspars, pyrite, and organic matter. Average clay-mineral contents are less at Benken (54 wt.%) than at Mont Terri (66 wt.%). In the oriented <2 μm fraction, the 10 Å peak can be decomposed into: (1) an ordered illite-smectite mixed-layer phase with 70−85% of illite layers; (2) a well crystallized illite (probably including a proportion of detrital mica) that only shows a slight shift of the peak upon ethylene-glycol solvation; and (3) a poorly crystallized illite with a broad 001 peak. A narrow peak at 14.3−14.5 Å indicates well crystallized chlorite, and a limited shift upon solvation is interpreted to be due to <10% interstratified smectite layers. Peaks around 7 and 3.5 Å could be decomposed into contributions from chlorite and kaolinite. Analysis of the >10 μm fraction
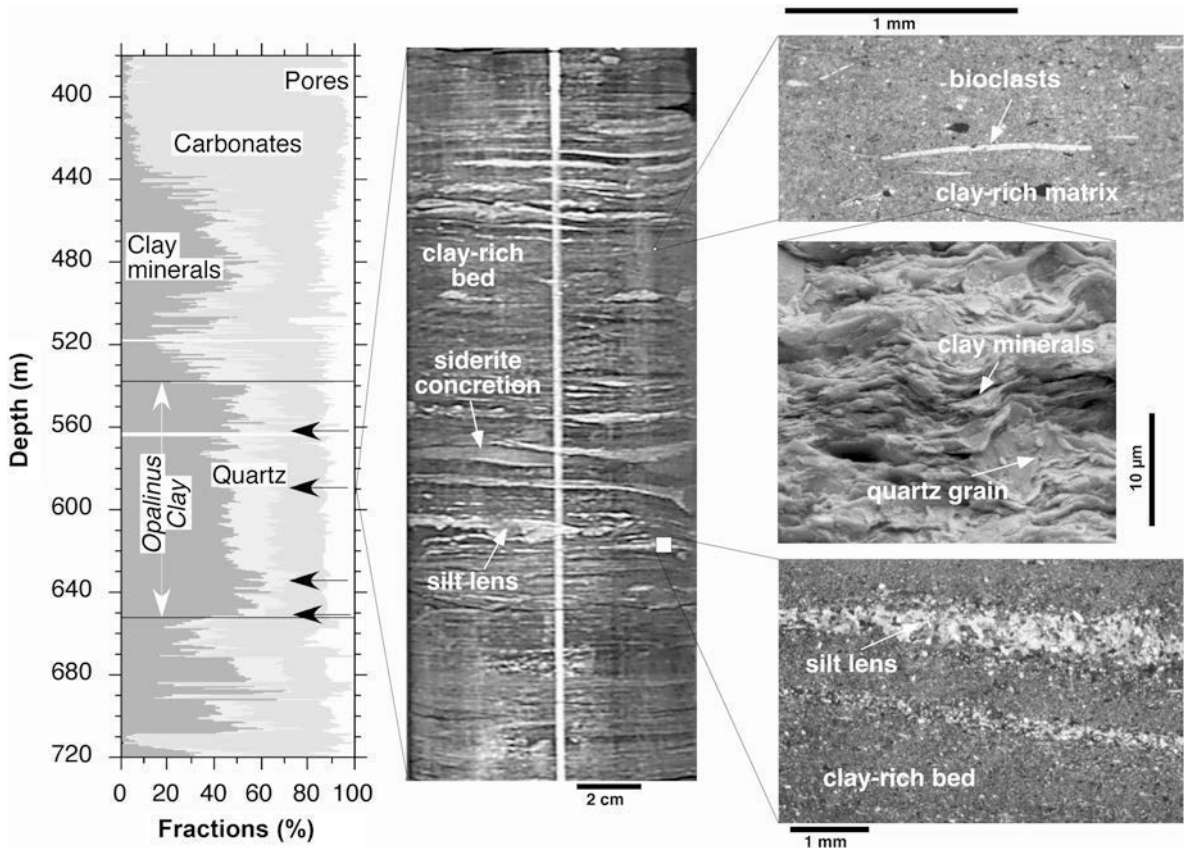

Figure 2. Stratigraphy and mineral composition of Benken Opalinus clay with sample locations. To the right are typical microstructures. Black arrows indicate sample locations.

yielded sharper (*i.e.* smaller peak width at half maximum intensity) peaks for well crystallized illite and for chlorite. The greater peak intensity for chlorite indicates that this phase has a larger average grain size than the other clay minerals. It possibly represents altered detrital biotite. Only very minor differences are observed between Benken and Mont Terri. At Benken, the peak widths at half maximum intensity for poorly crystallized illite and for chlorite are slightly greater.

Four samples were obtained from the Benken drill-hole at different depths, and two samples from the Mont Terri Laboratory (Table 1). In contrast to the horizontally bedded and largely undisturbed setting at Benken, the Opalinus Clay at Mont Terri is deformed and comprises part of the thin-skinned fold belt of the Jura Mountains. One of the Mont Terri samples was taken from a largely undisturbed domain adjacent to a brittle fault and the other from the fault itself (Borehole BSF-006, 1.2 m depth; Swiss Coordinates: 579.8/246.9, Figure 3). The sedimentary facies and mineralogical composition of the Opalinus Clay at Mont Terri is analogous to that at Benken. Water-accessible porosity is slightly greater at Mont Terri (16%) than at Benken (12%), consistent with the lesser degree of compaction to which the formation was subjected during burial. According to basin modeling, the maximum burial at Benken was to 1650 m, but only 1350 m at Mont Terri (Mazurek *et al.*, 2006). This means that the Opalinus Clay was subjected to a deeper geological burial than that of the Callovo-Oxfordian at Bure (800 m).

For the X-ray analysis, rock fragments were first embedded in epoxy. Slabs of 20 mm × 10 mm × 2 mm were cut from core-plugs, with the long dimension more or less perpendicular to the macroscopic bedding. After that, samples were mounted in an aluminum holder for stability. In the samples from the Callovo-Oxfordian (MHM-URL), conventional analysis using an X-ray powder diffractometer was performed before and after glycolation and heat treatments to establish the presence

of chlorite. This experiment showed no shift of the 14 Å peak upon glycolation and heating, thus confirming the presence of chlorite. For the rest of the experimental work, we used synchrotron X-rays as described in the next section.

TEXTURE ANALYSIS

Clay minerals are fine-grained and poorly crystalline, and conventional analysis with X-ray pole figure goniometry gives only limited information. An X-ray technique, in transmission geometry, has been developed to measure pole figures of basal planes of layer silicates and was successfully applied to slates (*e.g.* Oertel, 1983; Ho *et al.*, 1995; Jacob *et al.*, 2000). Shales are generally composed of several layer silicate minerals such as illite, kaolinite, smectite, and chlorite. These minerals often show peak broadening due to particle size, stacking disorder, polytypism, interlayering, and microstrain (*e.g.* Guggenheim *et al.*, 2002). In addition, other minerals are present: mostly quartz and carbonates (calcite, ankerite, siderite), and some minor phases such as feldspars and pyrite. Due to these factors, a powder X-ray diffraction (XRD) pattern is often difficult to analyse and interpret, though some results have been obtained, relying on basal reflections at low diffraction angles (Aplin *et al.*, 2006; Ho *et al.*, 1999; Solum *et al.*, 2003, 2005; Valcke *et al.*, 2006; Yan *et al.*, 2001). Because of multiple overlaps, individual peaks can often not be identified. This led us to develop a different technique which we have applied previously to high-pressure phases in a diamond-anvil cell (Wenk *et al.*, 2004): hard synchrotron X-rays were combined with the Rietveld method for image analysis. This method uses the whole diffraction spectrum, rather than an individual diffraction peak.

The advantages of a synchrotron X-ray-source are: high brilliance, a focused beam, and, for hard X-rays (high energy, short wavelengths), significant sample penetration without major absorption, comparable to
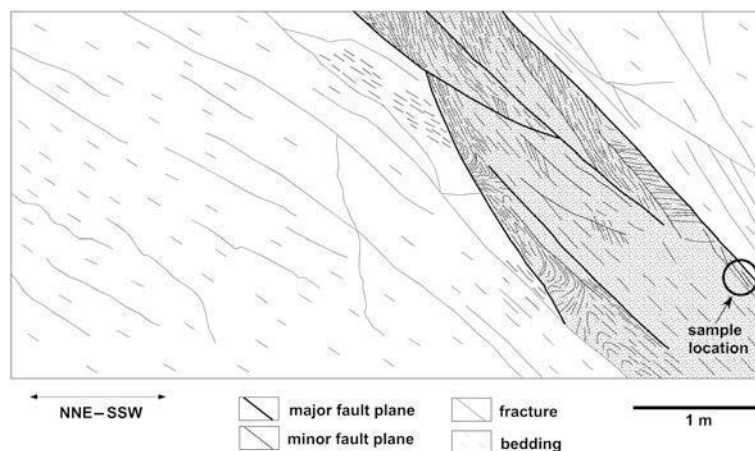

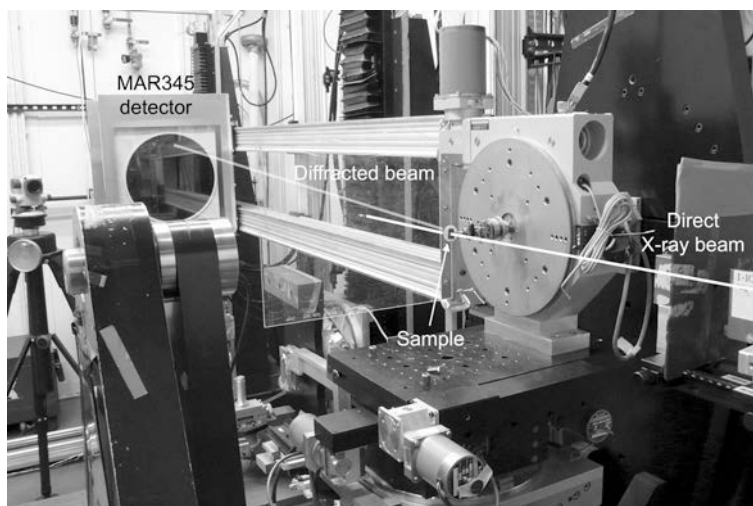Figure 3. Location of the Mont Terri samples in a fault zone.

Figure 4. Experimental setup at beamline 11-ID-C of APS with a sample mounted on the goniometer and an image plate detector.

neutrons. The use of 2-dimensional detectors such as CCD (Charged Coupled Device) cameras or image plates permits fast and reliable data collection. See Wenk *et al.* (2007) for details of the experimental procedure.

The shale samples were measured at the high-energy beamline BESSRC 11-ID-C at APS (Advanced Photon Source) of Argonne National Laboratory, with a monochromatic wavelength of 0.107863 Å. The beam size was 1 mm, and the sample-to-detector distance was ~2 m. The sample slabs were mounted on a metal rod approximately perpendicular to the bedding plane and parallel to the horizontal axis of the goniometer (Figure 4). Images were recorded with a Mar345 image plate detector (3450×3450 pixels). During data collection the sample was translated parallel to the horizontal axis over five spots in 2 mm increments in order to obtain a representative average. As the microstructures in Figures 1−2 suggest, there is considerable local heterogeneity in the samples and averaging is essential to minimize statistical artifacts. The counting time per image was 1000 s. A typical diffraction image of the Mont Terri 1 shale is shown in Figure 5. The intensity variations along most of the Debye rings immediately reveal the presence of texture. The variations are more pronounced for layer-silicate phases and less for calcite and particularly quartz. The preferred orientation is more evident in Figure 6 where the four Benken samples are compared and plotted as 'unrolled' 2D maps with azimuthal angle as ordinate. This was achieved using the *Fit2D* software (Hammersley, 1998). Quartz shows no preferred orientation (uniform intensity) and calcite shows moderate preferred orientation. Diffraction lines for layer silicates are smooth, while those for quartz and calcite are spotty, indicative of coarser grain size. From the images it is clear that clay minerals in samples 3 and 4 (Figure 6c,d) are more strongly oriented than in samples 1 and 2 (Figure 6a,b). Notice the diffuseness

of the (00*l*) diffraction peaks along 2θ, particularly for illite (all visible reflections up to 1.3º2θ are 00*l* reflections of the various layer silicates). This diffuseness is due to interlayering (illite-smectite), polytypism, and stacking disorder.

Images were recorded at seven different ω tilt angles, rotating the samples around the horizontal axis in 15º increments (−45º, −30º, −15º, 0º, 15º, 30º, 45º). The rotation axis is close to the bedding plane normal and in the 0º tilt position the sample slab is perpendicular to the beam. Combining images at different tilt angles provides more pole figure coverage for texture analysis (Figure 7). Using this geometry, all images intersect
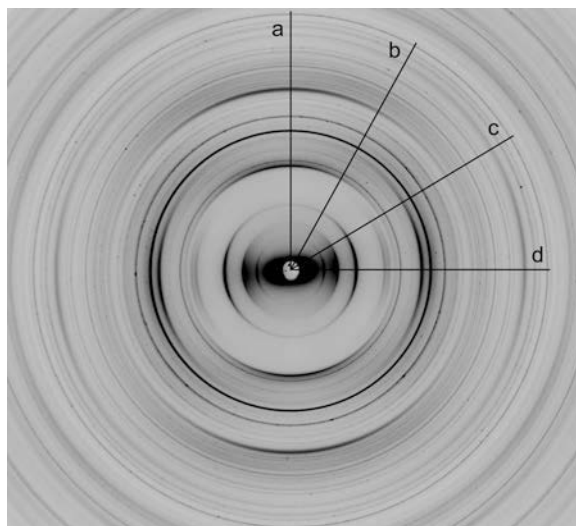

Figure 5. Diffraction image showing the strong preferred orientation of clay minerals in sample Mont Terri 1. The lines indicate the positions used to obtain the spectra illustrated in Figure 8.
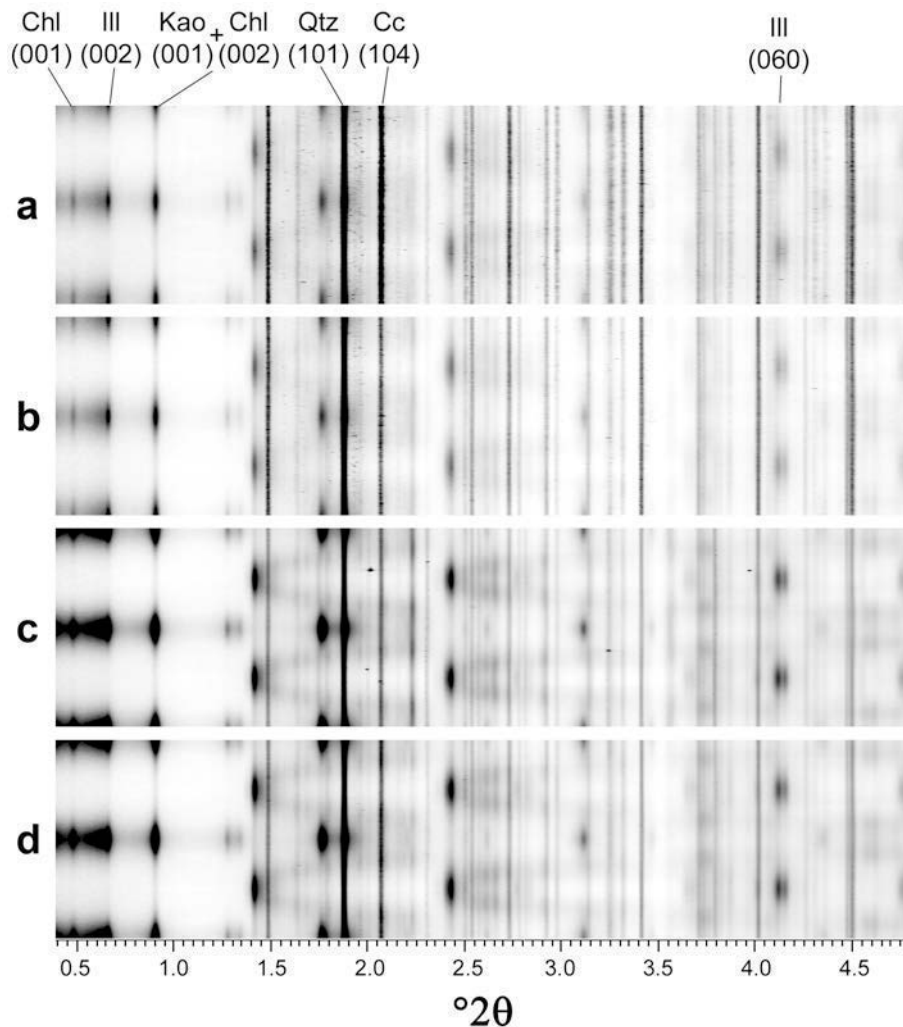
Figure 6. 2D plots of the four Benken samples with increasing depth as a function of diffraction image azimuth: the increase in texture strength is expressed in intensity variations. Some diffraction peaks are identified. A spotty pattern, *e.g.* for quartz and calcite, indicates larger grain size.

near the strong (001) maximum of layer silicates perpendicular to the bedding plane.

After collecting the data, the images were further processed using *Fit2D*. First, a CeO_2 powder standard was used to calibrate the sample-to-detector distance and orientation. These parameters were then kept constant for the processing of shale images. For each shale image, the image center was refined and then the image was divided into 15° azimuthal sectors and integrated over each sector to obtain spectra such as those shown in Figure 8, resulting in 24 spectra for each 2D image (esg files). These spectra, each representing differently oriented lattice planes (*i.e.* one spot on the lines of Figure 7), were then exported from *Fit2D* and used in the Rietveld refinement.

The Rietveld method (Rietveld, 1969; Young, 1993) was developed for powder patterns. Contrary to conventional techniques that rely on individual diffraction peaks for structural and textural information, the Rietveld method uses a continuous spectrum and is particularly adapted to polycrystalline samples with many overlapping peaks such as illustrated in Figure 8. It has been tested on powder samples of complex sedimentary rocks without preferred orientation (Hillier, 2000) and in the application of empirical corrections for texture effects (*e.g.* Dollase, 1986; Monecke *et al.*, 2001). The diffraction spectrum is expressed by a model function that depends on many parameters, including instrument geometry and resolution, scattering background, volume fractions of phases present, their crystal structure and microstructure, as well as the preferred orientation patterns. These parameters are then refined with a least-squares method to obtain an optimal fit between the model function and the experimental data. This fit is very good for the four spectra shown in Figure 8 (dots are experimental data
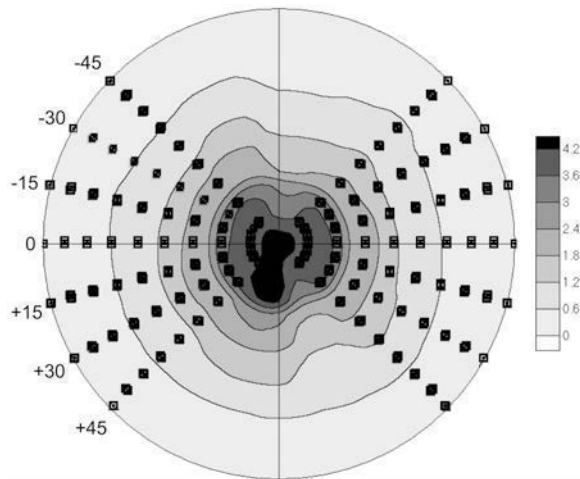
Figure 7. Pole figure coverage for the shale samples with seven measured images. The coverage pattern is superposed on a (001) illite pole figure. Equal area projection. The pole density contours are given in multiples of a random distribution (m.r.d.).

and the line is the model function). The four spectra are from different azimuthal sectors of an image (marked a, b, c, d, in Figure 5) and the relative changes in peak intensities are due to texture (of interest in this study). For the Rietveld refinement we used the program *MAUD* (Material Analysis Using Diffraction), a code written in *Java* (Lutterotti *et al.*, 1999). *MAUD* is unique among Rietveld codes in that it provides sophisticated methods

for quantitative texture analysis. The other Rietveld code with texture capabilities, *GSAS* (Larson and Von Dreele, 2004), only includes the harmonic method that is not very suitable for low-symmetry compounds and for strong textures. Using seven images provides $7 \times 24 = 168$ spectra that are used simultaneously in the Rietveld refinement. The *d* range used for the analysis is from 1.6 Å to 15 Å. Extending the *d* range to smaller *d* spacings did not improve results. If texture, rather than crystal structure, is of importance, the low-angle range with fewer peak overlaps is more significant in constraining the refinement.

As input, the Rietveld analysis requires the crystal structures for the mineral phases that are present. The clay structures applied in this study are those for kaolinite of Bish and Von Dreele (1989), illite-muscovite of Gualtieri (2000), based on Collins and Catlow (1992), and chlorite of Joswig *et al.* (1980). Note the complications with basal reflections of layer silicates. Kaolinite (001) (d = 7.2 Å, 0.83°2θ in Figure 8) is superposed on chlorite (002). The separation of these phases relies mainly on chlorite (001) (d = 14.3 Å, 0.42°2θ). With expansion tests we confirmed that this peak is indeed mainly chlorite. The illite (002) peak at 10.0 Å (0.6°2θ) has an asymmetric extension toward greater *d* spacings and this is due to illite-smectite interlayers and stacking disorder. This phase was modeled by adding to illite a hypothetical smectite structure (Viani *et al.* 2002; Grathoff and Moore, 1996).
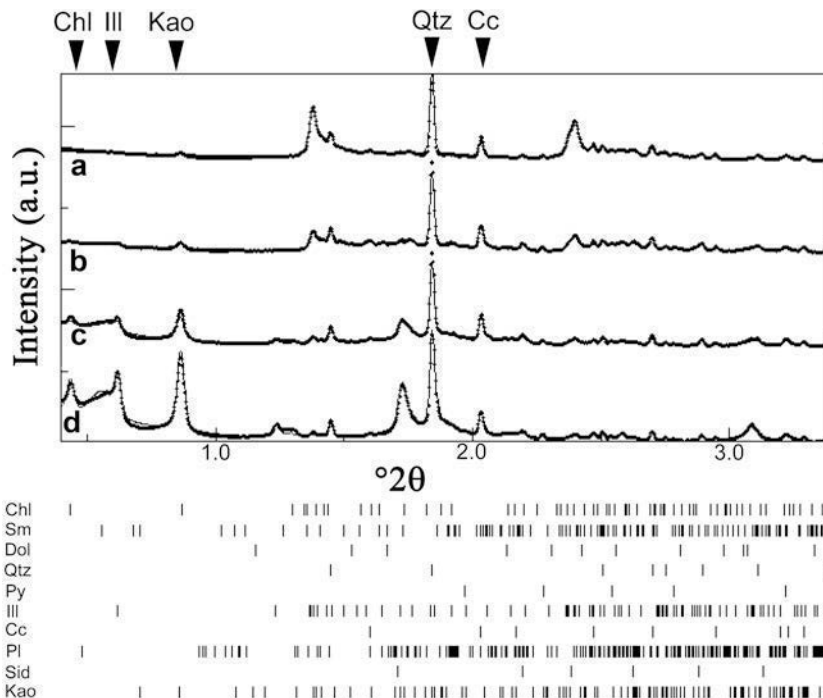

Figure 8. Four diffraction spectra of the Mont Terri 1 shale sample at different orientations (lines in Figure 5). The diffraction peaks of the ten contributing minerals are shown below. The dot patterns are experimental data; the solid line is the Rietveld fit.

Clearly, there is considerable uncertainty about the illite-smectite structure (Stixrude and Peacor, 2002) but it turns out that texture results are fairly insensitive to those details. Quartz and calcite are major additional components. Minor phases included in the refinement are pyrite, ankerite, siderite, and plagioclase. These minor phases were not considered in the texture analysis.

First instrumental parameters such as the center of the ring, the background parameters (three for each spectrum) and the scale parameters (one for each image) were refined. The scale parameters take into account different absorption and effective sample volumes with tilt as well as fluctuations in beam intensity. The second step is to extract weight fractions for each phase (quantitative phase analysis) and refine structural-microstructural parameters, including lattice parameters and anisotropic crystallite size (Popa, 1998). The refinement of crystallite size and shape with the Popa model up to harmonic order 4 is simply a convenient fitting parameter in *MAUD* and may not have a significant physical meaning because, in clay minerals, line broadening is strongly influenced by stacking faults (*e.g.* Moore and Reynolds, 1997; Drits and Tchoubar, 1990; Sakharov *et al.*, 1999). In the future, this is certainly a consideration for improvements but requires software modifications. Atomic coordinates, site occupancies, and temperature factors were held constant because of the large number of variables and the low

symmetry of the phases. In the last step, the most significant in this work, a modified algorithm of the EWIMV routine related to WIMV (Williams-Imhof-Matthies-Vinel; Matthies and Vinel, 1982) but with arbitrary cell coverage was used for the texture analysis. This tomographic method, which works in direct space, is preferred to Fourier methods such as the harmonic algorithm. The continuous 3-dimensional OD is divided into a discrete cell structure with an angular resolution of 15º. In *MAUD* these cells vary greatly in volume, which is significant for strong textures. It turned out that for these shales a sample orientation with the layer silicate basal plane maximum close to the center of the pole figure (Figure 6) was essential and greatly improved the resolution. (This is achieved by setting both sample-position angles, χ and ω, to zero in *MAUD*). No sample symmetry was imposed. In some cases, at the very end of the refinement process, refinement of the crystal structure of the clay phases was necessary in order to obtain a better fit. Lattice parameters for major phases and a representative sample from each locality are listed in Table 2. Variations within the same sample group are close to the estimated standard deviations (e.s.d.). Changes from the initial values are minor, except for kaolinite which is systematically different. Note that the standard deviations in a Rietveld fit do not consider systematic errors and the actual e.s.d. may be considerably larger, especially for lattice parameters

Table 2. Lattice parameters (Å and º) for major phases in shale samples.

	Lattice parameters	Starting values	Bure	Benken	Mont Terri
Kaolinite					
	a	5.1554	5.2800(7)	5.3360(8)	5.3243(9)
	b	8.9448	8.831(1)	8.792(1)	8.783(1)
	c	7.4048	7.375(1)	7.3637(7)	7.379(1)
	α	91.7	93.22(1)	92.93(2)	93.81(2)
	β	104.862	103.04(1)	102.21(1)	102.09(2)
	γ	89.893	88.155(2)	88.23(3)	88.24(3)
Illite					
	a	5.2226	5.239(1)	5.241(1)	5.235(1)
	b	9.0183	9.042(1)	9.085(1)	9.086(1)
	c	20.143	20.254(2)	20.126(1)	20.160(1)
	β	95.665	95.18(1)	95.71(3)	95.61(1)
Chlorite					
	a	5.3266	5.3262(9)	5.326(1)	5.229(1)
	b	9.232	9.231(1)	9.231(1)	9.152(1)
	c	14.399	14.299(1)	14.299(1)	14.387(1)
	α	90	89.97(1)	89.97(1)	89.87(1)
	β	97.16	97.16(2)	97.16(1)	98.87(3)
	γ	90	90.04(2)	90.04(1)	90.15(2)
Quartz					
	a	4.9137	4.9162(1)	4.9176(1)	4.9173(1)
	c	5.4047	5.4032(1)	5.4084(1)	5.4081(1)
Calcite					
	a	4.988	4.9894(1)	4.9853(1)	4.9856(1)
	c	17.061	17.0883(2)	17.0675(3)	17.0817(2)

Standard deviations for the least significant digits are given in parentheses.

(McCusker *et al.*, 1999). The overall weighted residual index R_{wp}, calculated for Rietveld refinements, are listed in Table 3, with

$$R_{wp} = \left\{ \sum_i w_i \left[y_i(\text{obs}) - y_i(\text{calc}) \right]^2 / \sum_i w_i \left[y_i(\text{obs}) \right]^2 \right\}^{1/2}$$

(1)

where $y_i(\text{obs})$ is the observed intensity at step i, $y_i(\text{calc})$ its calculated intensity, and w_i the weight. For all the analyses, the errors are similar and indicate a good fit.

Orientation distributions for all phases were exported from *MAUD* and further processed in *BEARTEX* (Wenk *et al.*, 1998). In *BEARTEX* the OD was smoothed with a 7.5° filter to alleviate artifacts from the OD cell structure. Where necessary, the OD was rotated so that the bedding plane was in the equatorial plane, and from this, pole figures were calculated and plotted in equal area projection. Pole densities are normalized so that the integral over a pole figure is 1.0 and densities are expressed in multiples of a random distribution (m.r.d.). We show (001) and (010) pole figures for layer silicates. The OD is a full 3-dimensional distribution function and used for the calculation of physical properties.

RESULTS

All samples have a rather complex mineralogical composition as established by the Rietveld analysis (Table 3). The major constituents (>10 wt.%) are illite (illite-smectite), kaolinite, calcite, and quartz. Minor constituents (<10 wt.%) are chlorite, feldspars, ankerite, siderite, and pyrite. We have only included plagioclase in the analysis, though minor K-feldspar (0.2−2%) has been reported for the Opalinus Clay (Nagra, 2002). Separating accessory feldspars was beyond the resolution available. Samples of the Callovo-Oxfordian have about equal portions of illite, quartz, and calcite and

only minor kaolinite. The Opalinus Clay samples have similar proportions of illite and kaolinite. Benken samples are rather variable, with increased illite and kaolinite in the deeper parts. This is consistent with the general increase of the clay content with depth (see Figure 2, left). The Mont Terri samples are similar to the lower Benken samples, as also established in previous investigations (Nagra 2002).

The texture is obvious from the diffraction patterns (Figure 5), or even better in 'unrolled' diffraction patterns (Figure 6). However, a quantitative assessment of preferred orientation is only obtained with the Rietveld fit. For illite (illite-smectite), chlorite, kaolinite, calcite, and quartz, ODs were obtained, relating crystallite orientations to the sample coordinate system with a three-dimensional distribution function. From the ODs, pole figures for selected lattice planes were calculated. In this study we focused on layer-silicate minerals which show the most distinct textural features and illustrate them with (001) and (010) pole figures for all samples. (001) corresponds to poles of layer-silicate platelets. Quartz and calcite are also of interest since they contribute about half of the weight fraction but, as will become apparent, textures are weaker or random. For quartz we only illustrate *c* axes (0001) pole figures for selected samples. In the case of carbonates $r = (10\bar{1}4)$ (cleavage rhomb) pole figures are also of interest. Pole-figure maxima and minima are listed in Table 4 in units of m.r.d. We see immediately that in all samples quartz is close to random (≈ 1 m.r.d.) and that illite is strongly oriented with (001) maxima >3 m.r.d. and minima in some cases close to zero, *i.e.* statistically very few (001) poles in the bedding plane.

For the two samples of Callovo-Oxfordian from MHM-URL we show (001) and (010) pole figures of illite and kaolinite (Figure 9). Illite is the major clay mineral and (100) pole figures (Figure 9a) show a moderate texture (3.2−3.6 m.r.d.) with a substantial proportion of randomly oriented crystallites (the minimum is 0.2 m.r.d.). The distribution is more or less

Table 3. Weight fractions (%) of mineral phases considered in this study. Note that smectite is not a separate phase but occurs as an interstratified I-S phase.

	Kaol- inite	Illite	Smectite	Chlorite	Quartz	Calcite	Ankerite	Siderite	Plagio- clase	Pyrite	R_{wp} (%)
MHM-URL 1	2.0(1)	34.6(6)	1.7(1)	1.2(1)	25.9(5)	23.6(5)	3.7(1)	–	5.8(2)	1.3(1)	6.3
MHM-URL 2	4.6(1)	33.2(6)	2.0(1)	6.4(2)	22.0(5)	25.0(5)	3.2(1)	–	1.9(1)	1.4(1)	9.8
Benken 1	12.1(3)	16.9(3)	1.1(1)	2.7(1)	41.0(6)	22.8(5)	0.2(1)	–	1.7(1)	1.2(1)	7.4
Benken 2	16.6(4)	23.7(3)	1.5(1)	3.3(1)	41.6(6)	11.0(3)	0.2(1)	1.0(1)	0.9(1)	–	8.2
Benken 3	20.7(4)	37.7(5)	1.8(1)	5.3(2)	18.7(3)	7.5(2)	0.8(1)	3.9(2)	0.6(1)	2.8(1)	8.2
Benken 4	20.5(4)	34.5(5)	2.8(1)	5.3(2)	22.8(4)	10.8(3)	1.0(1)	0.3(2)	0.2(1)	1.4(1)	7.2
Mont Terri 1	26.7(5)	36.6(6)	1.8(1)	4.8(1)	17.6(3)	9.0(2)	0.3(1)	0.8(1)	0.6(1)	1.9(1)	8.2
Mont Terri 2	25.6(4)	30.7(5)	1.0(1)	3.6(1)	18.3(3)	17.4(3)	0.1(1)	1.2(1)	–	1.8(1)	6.2

Standard deviations, from the Rietveld refinement, for the least significant digit are given in parentheses. R_{wp} is the residual index of the Rietveld refinement.

Table 4. (001) pole figure maxima and minima of major phases in multiples of a random distribution.

	– Kaolinite –		– Illite –		– Calcite –		– Quartz –	
	max	min	max	min	max	min	max	min
MHM-URL 1	1.64	0.038	3.17	0.18	1.45	0.49	1.40	0.64
MHM-URL 2	3.75	0.43	3.62	0.17	1.58	0.60	1.23	0.71
Benken1	3.63	0.53	5.33	0.04	1.99	0.68	1.21	0.88
Benken2	3.50	0.50	4.66	0.07	2.03	0.46	1.39	0.77
Benken3	9.29	0.33	6.68	0.02	2.45	0.51	1.48	0.75
Benken4	7.84	0.30	6.31	0.02	3.14	0.62	1.51	0.72
Mont Terri1	6.29	0.30	8.48	0.05	3.05	0.41	1.29	0.81
Mont Terri2	2.77	0.37	4.99	0.15	4.39	0.22	1.42	0.67

axially symmetric about the normal to the bedding plane. We attribute deviations from axial symmetry to limitations of the analysis. (010) pole figures of illite show a uniform girdle with poles concentrated in the bedding plane. Kaolinite is subordinate (2−5%) and displays a weak texture in one sample and a sharp maximum superposed on a broad distribution in the second sample (Figure 9b). This sharp (001) concentration is not visible in the (010) pole figure and may be a statistical artifact. The texture of calcite (Figure 10a,e) and quartz (Figure 11a) is essentially random (see also Table 4).

For Opalinus Clay at Benken (Figure 12, Table 4), we can see that both kaolinite and illite show strong preferred orientation. Illite (001) pole figures display a peak perpendicular to the bedding (up to 6.7 m.r.d.) with no (001) poles in the bedding plane. For kaolinite this is different: there is a broad background of randomly oriented crystallites (mostly above 0.4 m.r.d.) and on top of that a sharp peak, particularly for the deeper samples (Benken 3 and 4; up to 9.3 m.r.d.). This is also evident in the diffraction images with considerable diffuseness for kaolinite at all azimuths (Figure 6). The shallower samples (Benken 1 and 2) have a weaker texture than the deeper samples (Benken 3 and Benken 4), probably due to the greater proportion of clay minerals in the whole rock in the deeper samples. For the Benken 1 sample, we show in Figure 13 (001) pole figures of five different minerals with the same pole density scale. This shows most clearly which are the main minerals contributing to texture and thus to anisotropy. Chlorite and illite (illite-smectite) have very strong textures, kaolinite and calcite are intermediate, and quartz is random (see also Figure 11b). Contrary to Callovo-Oxfordian shales, the Benken samples have calcite with a distinct texture with *c* axes perpendicular to the bedding plane (Figure 10b,f).

The Mont Terri 1 sample resembles the Benken 3 and 4 samples, with strong axisymmetrical textures of kaolinite (6.3 m.r.d.) and illite (8.5 m.r.d.) (Figure 14), as well as calcite (Figure 10c,g). Quartz is also random here (Figure 11c). The Mont Terri 2 sample is from a brittle shear zone and shows a weaker and less symmetrical texture for layer silicates (2.8 m.r.d. for kaolinite and 5 m.r.d. for illite) but a stronger texture for
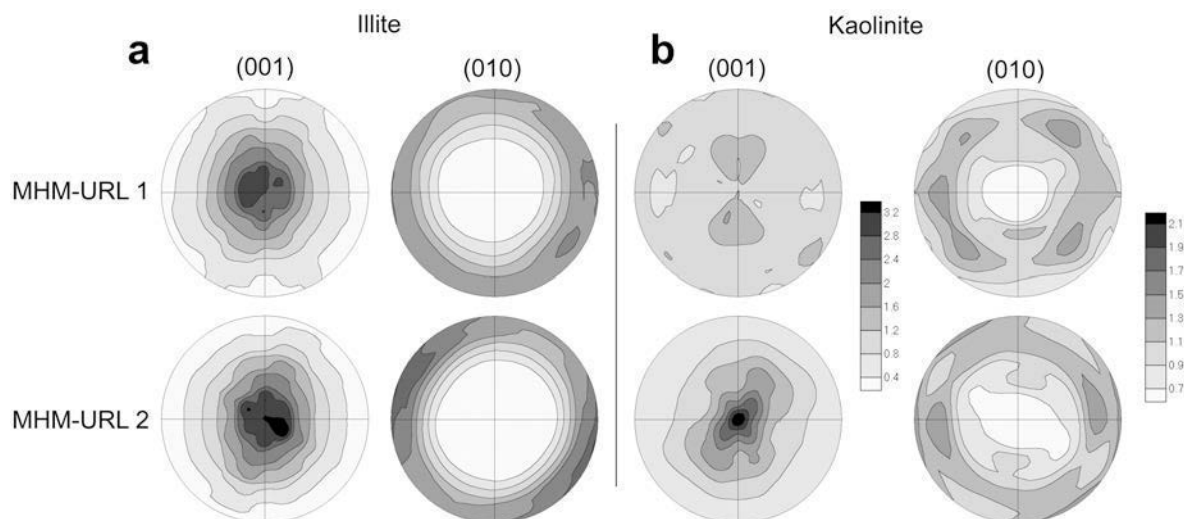

Figure 9. (001) and (010) pole figures of illite and kaolinite of the Bure (MHM-URL) shales. Equal area projection. Different pole density scales are used for (001) and (010) pole figures (values in m.r.d.).
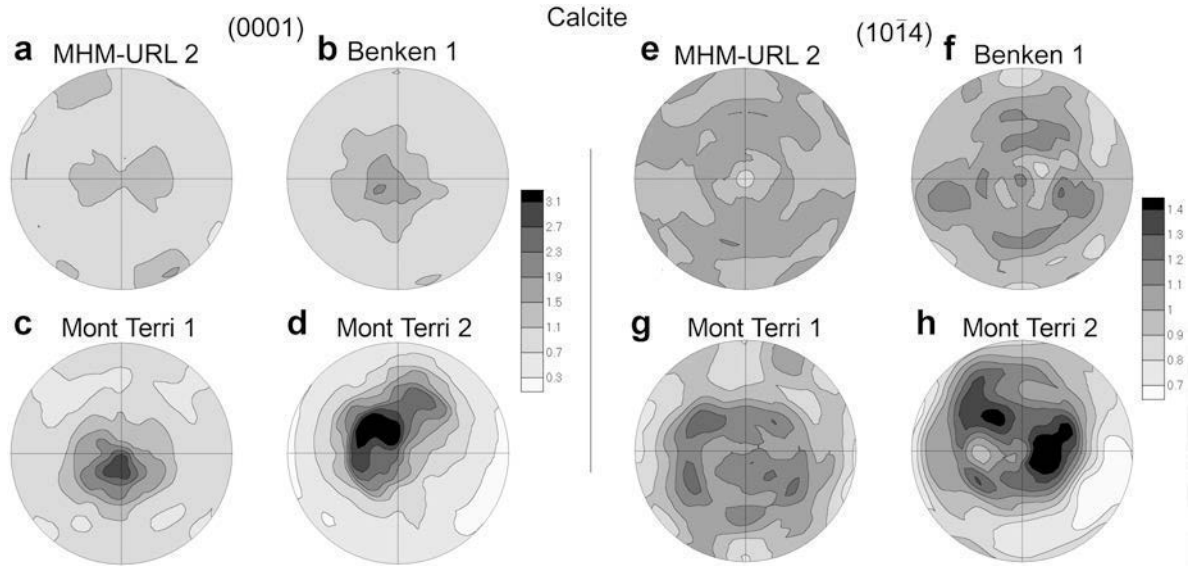
Figure 10. Pole figures for calcite in some of the shale samples. Of particular interest is the strong and asymmetric pattern for calcite from a shear zone (Mont Terri 2). Equal area projection.

calcite (4.4 m.r.d. Figure 10d) compared to Mont Terri 1 (3.1 m.r.d.; weakly deformed matrix adjacent to the fault). Furthermore, all Mont Terri 2 pole figures are distinctly asymmetrical with an inclined and elongated (001) maximum for layer silicates, (010) pole figures with a distinct maximum along the girdle (Figure 14), and particularly for calcite the (0001) maximum does not coincide with the layer silicate (001) maximum, and (10$\bar{1}$4) pole figures display a sharp asymmetric maximum (Figure 10h).

POLYCRYSTAL ELASTIC PROPERTIES

Texture patterns are important in the context of anisotropy of macroscopic physical properties, such as geomechanical and solute transport properties. In the case of shales, anisotropy of elastic properties has been most intensely studied because of the significance in seismic prospecting. The elastic anisotropy depends on the orientation distribution of crystallites and their single-crystal elastic properties, as well as low-aspect-

ratio pores and pore-water content (Bayuk *et al.*, 2007; Hornby *et al.*, 1994; Schoenberg and Sayers, 1995; Thomsen, 1995). This latter contribution is beyond the scope of this study, but we will address the intrinsic crystal contribution.

Polycrystal elastic properties can be obtained by averaging single crystal properties over the OD (Bunge, 1985). Apart from two recent studies (Lonardelli *et al.*, 2007; Wenk *et al.*, 2007) all previous work on shale anisotropy relied either on model functions (Hornby *et al.*, 1994; Sayers, 1994) or (00*l*) pole figures of layer silicates (Valcke *et al.*, 2006). This is an approximation because it assumes that *a* axes spin freely about the *c* axis which may not be the case in triclinic kaolinite and monoclinic illite. Unfortunately, the elastic properties of clay minerals are still poorly known (Katahara, 1996; Chen and Evans, 2006) and for this study we have used for illite and chlorite, experimental elastic stiffness moduli of muscovite measured with Brillouin scattering (Vaughan and Guggenheim, 1986), and for kaolinite, elastic constants derived from first-principles studies
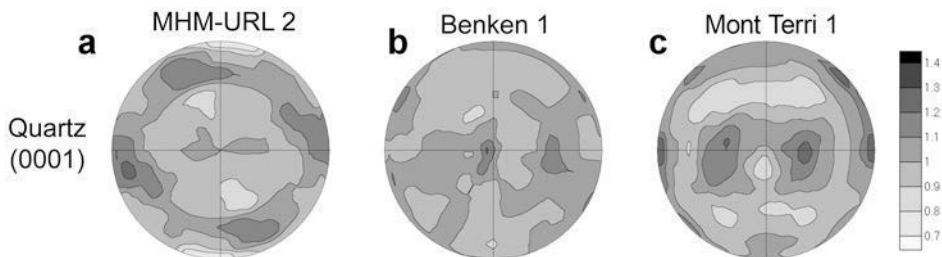

Figure 11. (0001) Pole figures of quartz for selected shale samples. The distribution is essentially random. Equal area projection; pole density contours in m.r.d.
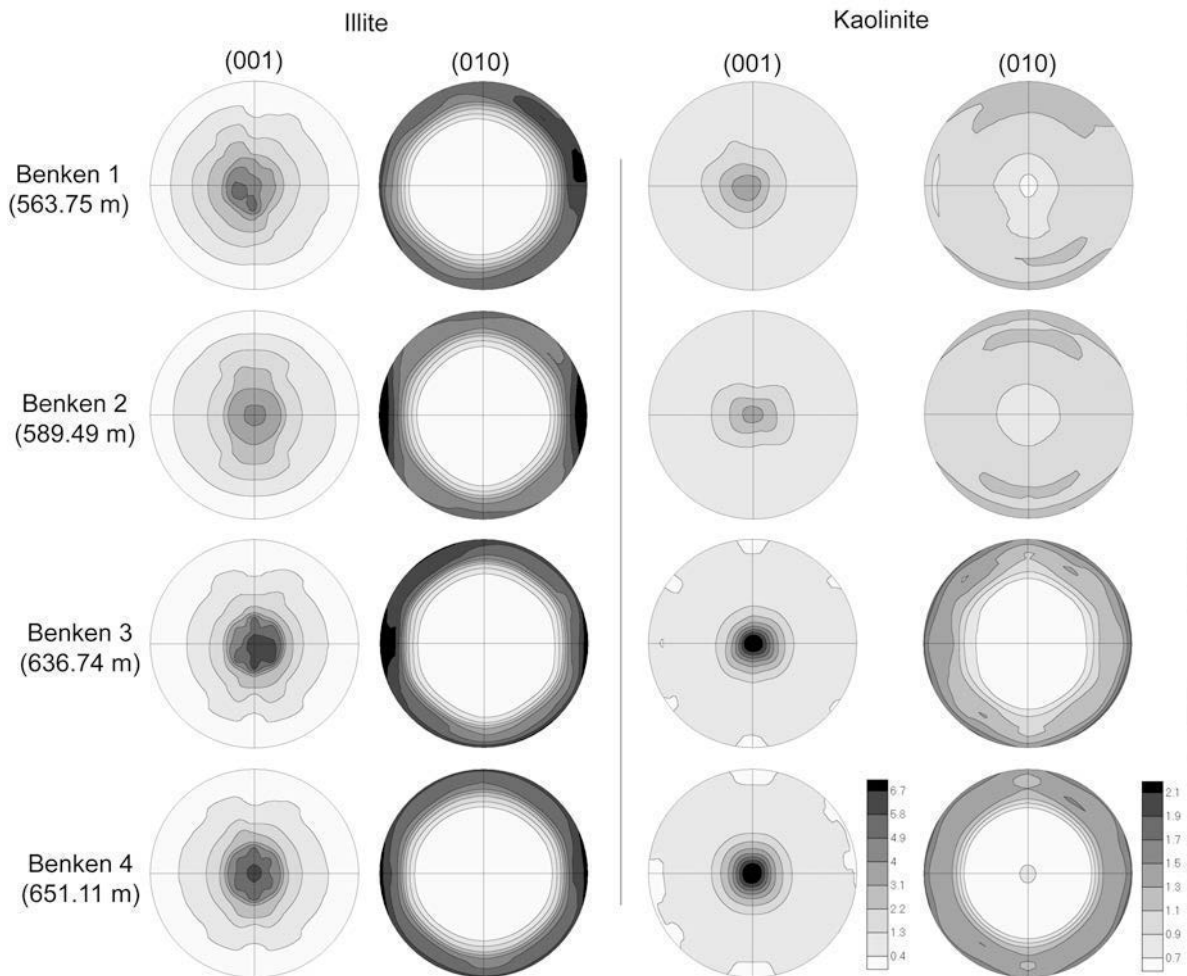
Figure 12. Illite and kaolinite (001) and (010) pole figures of the four Benken samples with increasing depth. Equal area projection; pole density contours in m.r.d.

(Sato *et al.*, 2005). Muscovite is treated as monoclinic and kaolinite as triclinic. For calcite we used elastic constants from Chen *et al.* (2001) and for quartz those from Heyliger *et al.* (2002).

   Various averaging schemes are used: the Voigt and Reuss averages provide upper and lower bounds, assuming uniform strain and uniform stress, respectively, throughout the textured aggregate. A geometric mean averaging is intermediate (Matthies and Humbert, 1993) and is the method applied in our calculations to obtain aggregate elastic tensors. We simplify the problem by first rotating the sample in *BEARTEX* using the program CSEC so that the (001) maximum coincides exactly with the center of the pole figure. Then we impose axial symmetry on the OD. For axially symmetrical aggregates, the elastic tensor is reduced to five independent stiffness coefficients, C_{11}, C_{13}, C_{33}, C_{44}, and C_{66} (in Voigt notation). These polycrystal stiffness coefficients are listed in Table 5 for the various phases. Notice that for quartz $C_{11} \approx C_{33}$ and $C_{44} \approx C_{66}$,

indicating isotropy. Polycrystal tensors for individual phases are then averaged by weight fractions (renormalizing to the major phases) to obtain an approximation of the bulk elastic tensor of the material. Layer silicates and calcite, the phases with significant preferred orientation, have both $C_{11} > C_{33}$ and thus their contributions add to anisotropy. This averaging is very simple, and does not take grain shapes, grain contacts, or oriented pores into account. The results are intermediate between the largest and smallest coefficients for the individual phases.

   From aggregate elastic constants (the five stiffness coefficients) and density we can then calculate aggregate phase velocities in different directions using the Christoffel transformation (V_p, V_{s1}, and V_{s2}) and anisotropies for p-waves ($V_p = 200\%$ ($V_{p\,max} - V_{p\,min}$)/($V_{p\,max} + V_{p\,min}$)) and shear-wave splitting ($dV_s = 2(V_{s1} - V_{s2})/(V_{s1} + V_{s2})$) as well as Thomsen parameters (1986) (using the program *VELO* in *BEARTEX*). Figure 15 shows the velocity variations as a function of angle to the bedding plane for individual phases of the sample Benken 3
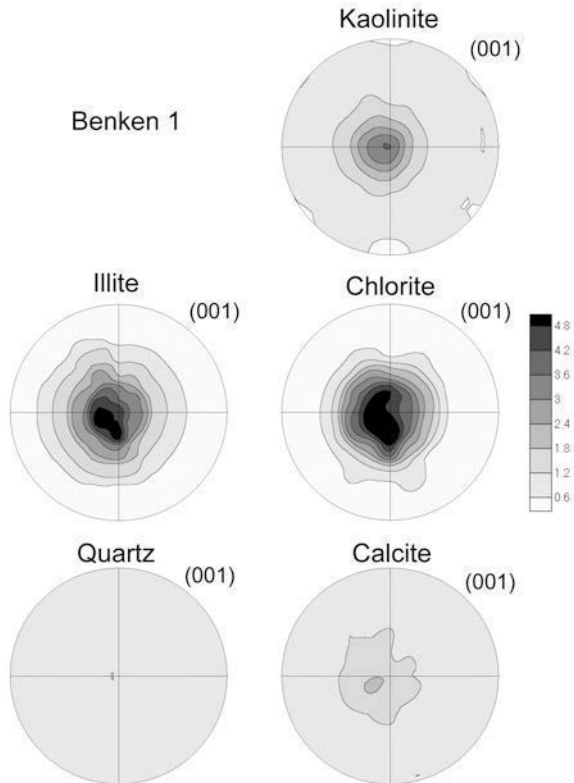
Figure 13. Pole figures of kaolinite, illite, chlorite, quartz, and calcite of the Benken 1 sample, all plotted with the same pole density scale (m.r.d.).

pies are also listed in Table 5. Anisotropies are least for the samples from MHM-URL (8−9%) and greatest for the deepest sample from Benken (21−22%).

To summarize our findings, we have obtained Thomsen anisotropy parameters ε ($\varepsilon = (C_{11}-C_{33})/2C_{33}$) and δ ($\delta = [(C_{12} + C_{14})^2 -(C_{33}-C_{44})^2]/[2C_{33}(C_{33}-C_{44})]$) (Thomsen, 1986) that are widely used in exploration geophysics (Wang, 2002) and the distribution for all phases in all samples is shown in Figure 16a. The value of δ is positive, except for quartz and $\varepsilon > \delta$, though only marginally, thus approximating elliptical anisotropy. The values for ε range between 0.08 and 0.28, comparable to a wide range of shales (Vernik and Liu, 1997; Vernik and Nur, 1992; Wang, 2002). In Figure 16b we plot minimum and maximum p-velocity values, again for all samples and all phases. The dashed line infers isotropy and quartz clusters near this line. Calcite spreads from isotropy towards anisotropy, while kaolinite and illite are highly anisotropic. The polyphase average is intermediate.

DISCUSSION

In this report, we apply a new method, designed for the study of preferred orientation of minerals, to shales composed of several phases. A quantitative description of preferred orientation requires determination of a three-dimensional OD which relates the orientation of crystallites to sample coordinates. With this distribution one can then model anisotropy of physical properties. Diffraction methods have been used extensively to measure texture but in the case of complex materials such as shales, conventional methods such as pole-figure diffractometry in transmission can at best determine pole figures of (00*l*) reflections of layer silicates, which are not sufficient to constrain the OD. Furthermore, due to

(Figure 15 a,b) and for polyphase averages for all samples (Figure 15 c,d). Note that even though calcite is oriented, its contribution to polyphase anisotropy is minimal. The greatest p-wave velocities are in the bedding plane, as well as the greatest shearwave splitting. Maximum and minimum p-wave velocities and corresponding anisotro-
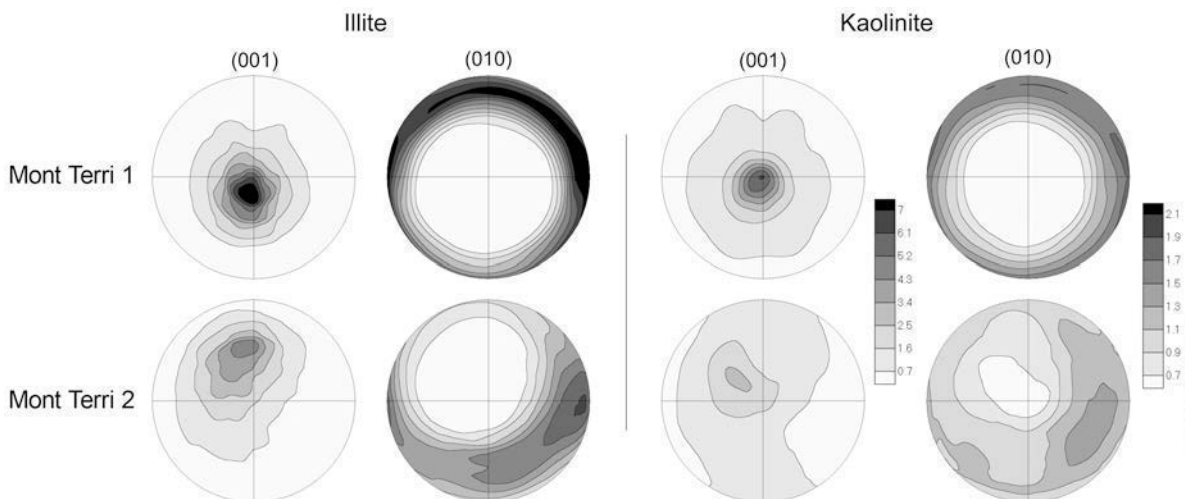

Figure 14. Illite and kaolinite pole figures of the two Mont Terri samples. A different density scale is used for the (001) and (010) pole figures (values in m.r.d.).

Table 5. Stiffness tensor coefficients (geometric mean) of selected minerals in shale samples, assuming axial symmetry, calculated maximum and minimum p-wave velocities (km/s), velocity anisotropy (%) as well as Thomsen parameters, ε and δ.

	C_{11}	C_{13}	C_{33}	C_{44}	C_{66}	Vp max	Vp min	Vp aniso	ε	δ
MHM-URL 1										
Kaolinite	94.8	13.1	90.9	38.8	40.8	6.0	5.9	2.1	0.022	−0.002
Illite	121.3	36.5	82.4	30.7	41.3	6.6	5.5	19.2	0.235	0.215
Quartz	96.9	8.3	96.2	44.6	44.4	6.1	6.0	0.5	0.004	0.013
Calcite	130.8	51.3	128.5	38.9	39.8	6.9	6.9	0.9	0.009	0.005
Polyphase	115.8	31.4	99.1	37.3	41.9	6.5	6.0	7.8	0.084	0.072
MHM-URL 2										
Kaolinite	109.3	11.7	69.5	35.9	46.7	6.4	5.1	22.5	0.286	0.243
Illite	123.2	36.3	80.3	30.2	42.2	6.7	5.4	21.3	0.267	0.239
Quartz	96.9	8.2	96.4	44.5	44.4	6.0	6.0	0.3	0.003	0.008
Calcite	130.0	51.5	129.2	39.3	39.4	6.9	6.9	0.3	0.003	0.007
Polyphase	117.6	32.1	97.9	36.8	42.2	6.6	6.0	9.2	0.101	0.085
Benken 1										
Kaolinite	109.5	11.3	72.0	35.0	47.3	6.4	5.2	20.9	0.260	0.143
Illite	129.6	35.5	74.7	28.6	45.2	6.9	5.2	27.4	0.368	0.289
Quartz	97.3	7.5	98.1	43.8	44.5	6.1	6.0	0.9	−0.004	−0.029
Calcite	132.2	51.5	125.7	38.5	40.7	7.0	6.8	2.5	0.026	0.022
Polyphase	113.2	23.7	96.9	38.6	44.1	6.5	6.0	7.8	0.084	0.042
Benken 2										
Kaolinite	107.6	11.7	73.2	35.6	46.5	6.4	5.3	19.2	0.235	0.152
Illite	127.7	35.8	76.2	29.1	44.3	6.8	5.3	25.6	0.338	0.277
Quartz	97.2	7.5	98.1	43.9	44.5	6.1	6.0	0.8	−0.004	−0.028
Calcite	133.7	52.0	122.0	38.3	41.7	7.0	6.7	4.6	0.048	0.056
Polyphase	111.1	20.6	90.7	38.0	44.5	6.4	5.8	10.1	0.113	0.068
Benken 3										
Kaolinite	121.5	9.1	61.9	32.3	51.8	6.8	4.8	33.4	0.482	0.230
Illite	135.6	34.5	71.1	27.0	47.9	7.0	5.1	32.0	0.454	0.292
Quartz	97.8	6.9	99.3	43.2	44.7	6.1	6.0	1.8	−0.008	−0.057
Calcite	133.0	52.5	121.3	38.9	41.4	7.0	6.7	4.6	0.048	0.079
Polyphase	123.5	23.5	79.3	32.9	47.6	6.8	5.4	22.1	0.279	0.141
Benken 4										
Kaolinite	126.4	8.5	57.8	31.6	53.6	6.9	4.7	38.6	0.592	0.304
Illite	134.7	34.7	71.5	27.3	47.5	7.0	5.1	31.4	0.443	0.298
Quartz	97.8	6.8	99.4	43.2	44.7	6.1	6.0	1.8	−0.008	−0.060
Calcite	134.0	52.2	121.1	38.3	41.9	7.0	6.7	5.1	0.053	0.067
Polyphase	123.3	23.5	81.2	33.6	47.6	6.8	5.5	20.8	0.259	0.129
Mont Terri 1										
Kaolinite	120.3	9.5	61.8	33.0	51.1	6.8	4.8	33.0	0.474	0.275
Illite	134.4	34.7	71.7	27.3	47.4	7.0	5.1	31.1	0.437	0.293
Quartz	97.3	7.6	97.9	43.9	44.5	6.1	6.0	0.8	−0.004	−0.026
Calcite	134.4	52.3	120.0	38.3	42.2	7.0	6.7	5.7	0.060	0.078
Polyphase	122.8	23.4	78.5	33.4	47.4	6.7	5.4	22.3	0.283	0.167
Mont Terri 2										
Kaolinite	107.8	11.9	71.7	36.0	46.3	6.4	5.2	20.3	0.252	0.201
Illite	124.6	36.3	78.6	30.0	42.9	6.7	5.3	23.0	0.293	0.266
Quartz	97.3	7.6	97.7	43.9	44.6	6.1	6.0	0.6	−0.002	−0.023
Calcite	140.1	52.4	112.1	36.4	45.7	7.2	6.4	11.1	0.125	0.128
Polyphase	117.2	26.5	86.6	35.7	44.7	6.6	5.7	15.1	0.177	0.145

diffuse peaks and peak broadening during sample tilt, it is difficult to establish a background function without profile analysis, adding uncertainty to methods that rely on single-peak intensity measurements. In addition, stacking disorder affects mainly the diffuseness and asymmetry of basal peaks (00l), and (0k0) and (h00) reflections would be more informative but are overlapped with other reflections in the diffraction pattern. For all these reasons a full profile analysis with the Rietveld method is advantageous, though not trivial.
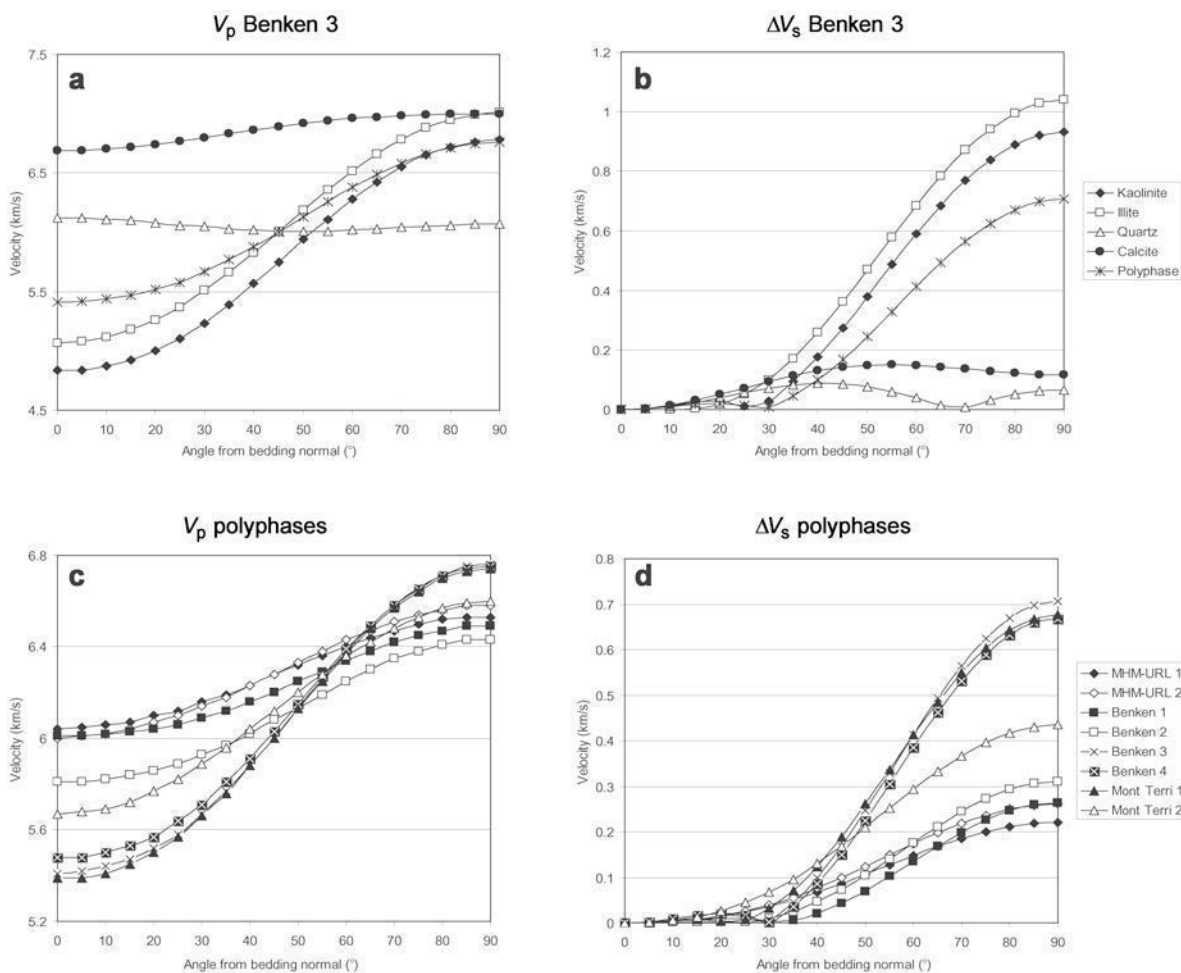
Figure 15. V_p (a,c) and ΔV_s (b,d) velocities for the various phases in the Benken 3 sample (a,b) and average aggregate velocities for all samples (c,d).

Here we apply hard synchrotron X-rays to produce diffraction images that can then be analyzed with the Rietveld method. It has been surprising how spectra, such as those shown in Figure 8 with 10 mineral phases and a multitude of overlapping diffraction peaks, can be deconvoluted to obtain textural information about the individual components. Furthermore, with hard X-rays, large volumes can be sampled (1 mm × 2 mm × 5 mm) which are representative of the locally heterogeneous rocks. The instrumentation to perform these experiments is available at many user facilities, such as the Advanced Photon Source at Argonne (used here), the Advanced Light Source in Berkeley, the Cornell High Energy Synchrotron Source in Ithaca, the European Synchrotron Research Facility in Grenoble, and at HASYLAB in Hamburg, and is used routinely for texture investigations. Clay researchers could take advantage of these opportunities.

Weight fractions of minerals calculated by the Rietveld method are compatible with results from the literature. However, quantitative phase analysis depends on the structural models, which for clays are often inaccurate because of the chemical variability and stacking disorder. This is especially true for phases such as montmorillonite, where the disorder has been modeled either by the use of $-a/3$ and $\pm b/3$ random shifts (Viani *et al.*, 2002), or using a turbostratic disorder model (Ufer *et al.*, 2004). For complex, clay-bearing multiphase materials, a wide range of approaches and techniques is used to get the most accurate weight fractions (*e.g.* Omotoso *et al.*, 2006). Because this study emphasizes preferred orientation, structural details are not of major importance.

Texture information was extracted for the major phases. All investigated samples show moderate to strong preferred orientation of layer silicates, particularly illite and kaolinite, but there are significant differences. In all samples, quartz has a random OD, and the calcite texture is variable. The texture is weakest in the Callovo-Oxfordian at Bure (MHM-URL), which is consistent with the limited geological burial to which this formation was subjected and with the weak
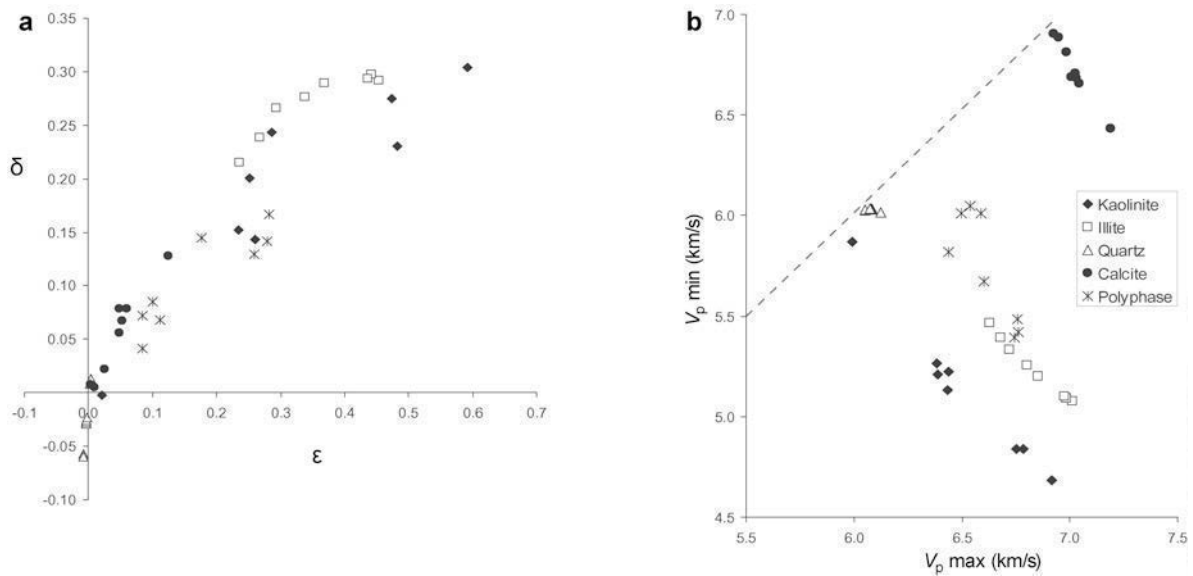
Figure 16. (a) Thomsen parameters ε and δ and (b) maximum and minimum p-wave velocities (km/s) for all samples and phases.

anisotropy of geomechanical and transport parameters (Table 6). No texture can be identified for calcite. Stronger preferred orientation is observed for the Opalinus Clay, mainly for clay minerals but also for calcite. Clay-rich samples (Benken 3, Benken 4) show a stronger texture than samples with fewer clay minerals (Benken 1, Benken 2), as shown in Figure 17. The chlorite texture is linked to that of illite, probably due to

Table 6. Experimental physical properties measured on shale samples with emphasis on anisotropy.

Parameter	Callovo-Oxfordian at Bure	Opalinus Clay at Benken	Opalinus Clay at Mont Terri
Bulk dry density (g/cm^3)	2.29±0.06[3]	2.43[4]	2.31[4]
Bulk saturated density (g/cm^3)	2.48±0.07[6]	2.52[4]	2.45[9]
Porosity (−)	0.14−0.18[2]	0.124[4]	0.16[5]
Vp normal to bedding (lab test) (km/s)	2.9±0.2[6]	3.03[4]	2.62[9]
Vs normal to bedding (lab test) (km/s)	1.6±0.1[6]	1.71[4]	1.51[9]
Vp parallel to bedding (lab test) (km/s)	3.4±0.1[6]	4.03[4]	3.03[9]
Vs parallel to bedding (lab test) (km/s)	1.9±0.1[6]	2.28[4]	1.96[9]
Uniaxial compressive strength normal to bedding (MPa)	21[1]	30[4]	16[9]
Undrained E (tangent) modulus normal to bedding (MPa)	4000±1470[1]	5500[4]	3600[9]
Anisotropy factor	1.2[1]	2.1[4]	1.6[9]
Cohesion normal to bedding at low confining pressure (MPa)	6.4[1]	8.6[4]	5[9]
Friction angle normal to bedding at low confining pressure (°)	29[1]	25[4]	25[9]
Swelling pressure normal to bedding (MPa)	1.0−3.0[1]	1.1[4]	1.2[9]
Swelling pressure parallel to bedding (MPa)	(anisotropy not measured)	0.15[4]	0.5[9]
Effective diffusion coefficient for HTO normal to bedding (m^2/s)	2.1E−11[2]	5.4E−12[7,8]	1.4E−11[7,8]
Effective diffusion coefficient for HTO parallel to bedding (m^2/s)	3.3E−11[2]	3.2E−11[7,8]	5.4E−11[7,8]
Hydraulic conductivity normal to bedding (m/s)	1E−14 to 6E−13[2]	6E−15 to 3E−14[4]	6E−14 to 1.2E−13[4]
Hydraulic conductivity parallel to bedding (m/s)	1E−14 to 1E−12[2]	1E−14 to 6E−14[4]	2E−14 to 2E−12[4]
Thermal conductivity normal to bedding (W/m/K)	1.3 ± 0.17[1]	1.26−1.70[4]	1.0−3.1
Thermal conductivity parallel to bedding (W/m/K)	1.9 ± 0.48[1]	2.04−3.22[4]	

Based on data from [1] Andra (2005c), [2] Andra (2005d), [3] Bauer *et al.* (1997), [4] Nagra (2002), [5] Pearson *et al.* (2003), [6] Rebours *et al.* (2007), [7] Van Loon *et al.* (2004), [8] Van Loon and Soler (2004), and [9] Bock (2001).
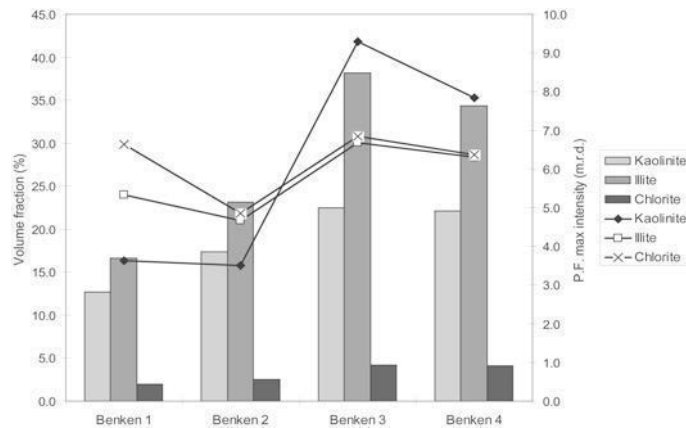
Figure 17. Shales from Benken drill hole. Plot shows maximum pole intensities for the clay phases (m.r.d.) and histograms with corresponding weight fractions.

their similar grain morphology. Kaolinite is more variable. From a mineralogical point of view, samples Benken 3 and Benken 4 are comparable to samples from Mont Terri. Remarkably, texture is clearly more developed at Benken when compared to Mont Terri 1, which is consistent with the deeper burial (and lower porosity) at Benken. The orientation of calcite with *c* axes perpendicular to the foliation plane is different from that observed in the Solnhofen limestone (Wenk *et al.* 1972) but consistent with low-temperature compression, suggesting that the orientation may be secondary and formed during compaction.

In clayey rocks, mainly composed of clay platelets that have been deposited in aqueous-marine environments, different stages can be distinguished. Initially, platelets are stacked fairly randomly like a house-of-cards, with much porosity. During compaction by overburden (axial compression), porosity diminishes and clay platelets become aligned. Sintubin (1994a) observed strengthening of the layer-silicate texture with increasing burial depth. The original sedimentary orientation pattern is then modified by deformation, generally resulting in a reduction of symmetry. A modified March (1932) model has been developed to quantify texture development during compaction (Oertel and Curtis, 1972), and to infer from the (001) layer-silicate pole figure maximum ρ_{max} (m.r.d.) the magnitude of the compaction strain $\varepsilon_c : \varepsilon_c = \sqrt{\rho_{max}} - 1$. With this expression and applying it to illite pole figure maxima of 3−8 m.r.d., we estimate compaction strains of between 0.7 and 1.8.

Two samples have been measured for the Opalinus Clay from Mont Terri, one from the weakly deformed rock matrix and one from an adjacent shear zone. All Mont Terri texture patterns are less symmetrical than those of the Benken samples and we attribute this to tectonic deformation. Compared to Mont Terri 1 (matrix), Mont Terri 2 (fault rock) displays weaker and asymmetrical texture patterns for kaolinite and illite. More significantly the calcite is enhanced (at 4.4. m.r.d.,

the strongest of all samples) and has a distinct asymmetric (10$\bar{1}$4) maximum. The calcite pole figures display monoclinic symmetry, consistent with shear deformation (Figure 10 d,h) and it is likely that these preferred orientation patterns developed through crystal plasticity under stress such as mechanical twinning.

There is not much quantitative information about preferred orientation in shales. Most studies on layer silicate textures have focused on slates and, in those, crystal alignment is considerably stronger (*e.g.* Oertel and Phakey, 1972, 16 m.r.d., Sintubin 1994b, 5−18 m.r.d.). Maximum (00*l*) pole densities for illite and kaolinite observed in this new study are similar to those reported for Zechstein shales (Sintubin 1994a, 4−6 m.r.d.), Gulf coast mudstones (Ho *et al.*, 1999, 2−7 m.r.d.), mudstones from Pennsylvania (Ho *et al.*, 1995, 2−5 m.r.d.), shales from Nigeria (Lonardelli *et al.*, 2007, 3−4 m.r.d.), and shales/siltstones from the North Sea (Valcke *et al.*, 2006, 3−5 m.r.d.). All these analyses, except that of Lonardelli *et al.* (2007), rely on conventional pole-figure diffractometry and only analyze a single layer-silicate basal diffraction peak. For reasons outlined above, we maintain that the full profile Rietveld analysis is more quantitative than analysis of a single, often partially overlapped, basal reflection peak. Furthermore, most shales are composed of several phases. Valcke *et al.* (2006) report analyses of quartz, dolomite, and siderite, measured by electron back-scatter diffraction. The pole figures are very spotty and maximum pole densities are small. They resemble in many ways our Figure 11 and suggest that there is no significant preferred orientation of these minerals.

Preferred orientation of minerals is an intrinsic contribution to anisotropy of elastic properties, of great interest in shales, and has been explored with acoustic methods for some of the samples investigated in this study (Table 6). While anisotropy of acoustic waves parallel and perpendicular to the bedding is similar for averaging predictions and experiments, the magnitude of calculated acoustic wave velocities is much greater. In

the model porosity, intergrain contacts are not considered and assumed single-crystal elastic properties may be too high. It is obvious, *e.g.* from Figure 15a, that kaolinite and illite dominate the anisotropy and the contribution from calcite, though significantly oriented, is much less.

Table 6 lists experimentally determined physical properties in the same samples. It illustrates anisotropy, not only for acoustic waves, but for thermal conductivity, hydraulic conductivity, effective diffusion, and swelling pressure as well. These experimental properties are less anisotropic for Callovo-Oxfordian shales than for Opalinus Clay. Experimental acoustic velocities are smaller and anisotropies are greater (Table 6) than those inferred from texture patterns (Table 5). The likely reason for this is that in our simple polyphase averaging, neither grain-shape effects nor intragrain porosity are taken into account; these would reduce elastic stiffness and thus reduce acoustic velocities (Hornby *et al.*, 1994; Ponte Castaneda and Willis 1995; Sayers, 1994, 2005; Bayuk *et al.*, 2007). Furthermore, we are using the elastic properties of muscovite for illite-smectite, which is obviously an upper limit. In the future, a more sophisticated averaging scheme needs to be employed which takes porosity and particle shape into account in a comprehensive fashion. Having quantitative orientation distributions of all phases we can now explore the influence of other factors on anisotropy of physical properties.

CONCLUSIONS

In this study, high-energy and high-intensity X-rays from a synchrotron source were used to obtain diffraction images that were then analyzed using the Rietveld method, with the primary aim to obtain quantitative information about the preferred orientation of clay minerals in shales. This method proved to be very powerful in separating diffraction patterns of multiple phases into separate components, and in determining the structural and textural features of each phase. The samples of Callovo-Oxfordian shale from Meuse/ Haute-Marne Underground Rock Laboratory at Bure, France, and of Opalinus clays from Benken and Mont Terri, Switzerland, show moderate to strong preferred orientation and the complexity of the orientation pattern is consistent with the geological history, particularly in the case of Mont Terri, where sedimentation and compaction were followed by tectonic deformation. The mineral orientation correlates with anisotropy of macroscopic properties such as acoustic-wave propagation and transport parameters.

ACKNOWLEDGMENTS

REFERENCES

Andra (2005a) Dossier 2005 Argile: Synthesis. Evaluation of the feasibility of a geological repository in an argillaceous formation. Andra, France (available at www.andra.fr).

Andra (2005b) Dossier 2005 Argile: Phenomenological evolution of a geological repository. Andra, France (available at www.andra.fr).

Andra (2005c) Dossier 2005 Argile: Référentiel du site de Meuse/Haute-Marne, Tome 2: Caractérisation comportementale du milieu géologique sous perturbation. Andra, France (available at www.andra.fr).

Andra (2005d) Dossier 2005 Argile: Référentiel du site de Meuse/Haute-Marne, Tome 1: Histoire géologique et état actuel. Andra, France (available at www.andra.fr).

Aplin, A.C., Matenaar, I.F., McCarty, D., and van der Pluijm, B.A. (2006) Influence of mechanical compaction and clay mineral diagenesis on the microfabric and pore-scale properties of deep water Gulf of Mexico mudstones. *Clays and Clay Minerals*, **54**, 501−515.

Banik, N.C. (1984) Velocity anisotropy of shales and depth estimation in the North Sea basin. *Geophysics*, **49**, 1411−1419.

Bauer, C., Pouya, A., and Ghoreychi, M. (1997) *Propriétés thermo-mécaniques des argilites silto-carbonatées de l'est*. Andra report BRP0G3S97-001.

Bayuk, I., Ammermann, M., and Chesnokov, E. (2007) Elastic moduli of anisotropic clay. *Geophysics*, **72**, D107−D117.

Bish, D.L. and Von Dreele, R.B. (1989) Rietveld refinement of non-hydrogen atomic positions in kaolinite. *Clays and Clay Minerals*, **37**, 289−296.

Bock, H. (2001) *Mont Terri Project. RA experiment: Rock mechanics analyses and synthesis; data report on rock mechanics*. Mont Terri Consortium, Technical Report TR 2000−02.

Bossart, P. and Thury, M. (2007) Research in the Mont Terri Rock Laboratory: Quo vadis? *Physics and Chemistry of the Earth*, **32**, 19−31.

Bunge, H.-J. (1985) Physical properties of polycrystals: Pp. 507−525 in: *Preferred Orientation in Deformed Metals and Rocks: An Introduction to Modern Texture Analysis* (H.R. Wenk, editor). Academic Press, Orlando, Florida, USA.

Chen, B. and Evans J.R.G. (2006) Elastic moduli of clay platelets. *Scripta Materialia*, **54**, 1581−1585.

Chen, C.-C., Lin, C.-C., Liu, L.-G., Sinogeikin, S.V., and Bass, J.D. (2001) Elasticity of single-crystal calcite and rhodochrosite by Brillouin spectroscopy. *American Mineralogist*, **86**, 1525−1529.

Claret, F., Sakharov, B.A., Drits, V.A., Velde, B., Meunier, A., Griffault, L., and Lanson, B. (2004) Clay minerals in the Meuse-Haute Marne underground laboratory (France): Possible influence of organic matter on clay mineral evolution. *Clays and Clay Minerals*, **52**, 515−532.

Collins D.R. and Catlow C.R.A. (1992) Computer simulation of structures and cohesive properties of micas. *American Mineralogist*, **77**, 1172−1181.

Crampin, S. (1981) A review of wave motion in anisotropic and cracked elastic media. *Wave Motion*, **3**, 242−391.

Delay, J., Vinsot, A., Krieguer, J.M., Rebours, H., and Armand, G. (2007) Making of the underground scientific experimental programme at the Meuse/Haute-Marne underground research laboratory, North Eastern France. *Physics and Chemistry of the Earth*, **32**, 2−18.

Dollase, W.A. (1986) Correction of intensities for preferred orientation in powder diffractometry: Application of the March model. *Journal of Applied Cystallography*, **19**, 267−272.

Drits, V.A. and Tchoubar, C. (1990) *X-ray diffraction by Disordered Lamellar Structures: Theory and Applications to Microdivided Silicates and Carbons*. Springer-Verlag, Berlin.

Esteban, L., Géraud, Y., and Bouchez, J.-L. (2007) Pore network connectivity anisotropy in Jurassic argillite specimens from eastern Paris Basin (France). *Physics and Chemistry of the Earth*, **32**, 161−169.

Gaucher, E., Robelin, C., Matray, J.M., Negrel, G., Gros, Y., Heitz, J.F., Vinsot, A., Rebours, H., Cassabagnere, A., and Bouchet, A. (2004) ANDRA underground research laboratory: interpretation of the mineralogical and geochemical data acquired in the Callovo-Oxfordian Formation by investigative drilling. *Physics and Chemistry of the Earth*, **29**, 55−77.

Gautschi, A. (2001) Hydrogeology of a fractured shale (Opalinus Clay): Implications for deep geological disposal of radioactive wastes. *Hydrogeological Journal*, **9**, 97−107.

Grathoff, G.H. and Moore, D.M. (1996) Illite polytype quantification using WILDFIRE calculated X-ray diffraction patterns. *Clays and Clay Minerals*, **44**, 835−842.

Gualtieri A.F. (2000) Accuracy of XRPD QPA using the combined Rietveld-RIR method. *Journal of Applied Crystallography*, **33**, 267−278.

Guggenheim, S., Bain, D.C., Bergaya, F., Brigatti, M.F., Drits, V.A., Eberl, D.D., Formoso, M.L.L., Galán, E., Merriman, R.J., Peacor, D.R., Stanjek, H., and Watanabe, T. (2002) Report of the Association Internationale pour l'Etude des Argiles (AIPA) Nomenclature Committee for 2001: Order, disorder and crystallinity in phyllosilicates and use of the 'crystallinity index'. *Clays and Clay Minerals*, **50**, 406−409.

Hammersley, A.P. (1998) *Fit2D*: V99.129 Reference Manual Version 3.1. Internal Report ESRF − 98 − HA01.

Heyliger, P., Ledbetter, H., and Kim, S. (2002) Elastic constants of natural quartz. *Journal of the Acoustical Society of America*, **114**, 644−650.

Hillier, S. (2000) Accurate quantitative analysis of clay and other minerals in sandstones by XRD; comparison of a Rietveld and a reference intensity ratio (RIR) method and the importance of sample preparation. *Clay Minerals*, **35**, 291−302.

Ho, N.C., Peacor, D.R., and Van der Pluijm, B.A. (1995) Reorientation mechanisms of phyllosilicates in the mudstone-to-slate transition at Lehigh Gap, Pennsylvania. *Journal of Structural Geology*, **17**, 345−356.

Ho, N.C., Peacor, D.R., and Van der Pluijm, B.A. (1999) Preferred orientation of phyllosilicates in Gulf Coast mudstones and relation to the smectite-illite transition. *Clays and Clay Minerals*, **47**, 485−504.

Homand, F., Shao, J.-F., Giraud, A., Auvray, C., and Hoxha, D. (2006) Petrofabric and mechanical properties of mudstones. *Comptes rendus Geoscience*, **338**, 882−891.

Hornby, B.E. (1998) Experimental laboratory determination of the dynamic elastic properties of wet, drained shales. *Journal of Geophysical Research*, **103**(B12), 29945−29964.

Hornby, B.E., Schwartz, L.M., and Hudson, J.A. (1994) Anisotropic effective-medium modelling of the elastic properties of shales. *Geophysics*, **59**, 1570−1583.

Jacob, G., Kisch, H.J., and van der Pluijm, B.A. (2000) The relationship of phyllosilicate preferred orientations, X-ray diffraction intensity ratios and c/b fissility ratios in metasedimentary rocks of the Helvetic zone of the Swiss Alps and the Caledonides of Jamtland, central western Sweden. *Journal of Structural Geology*, **22**, 245−258.

Johnston, J.E. and Christensen, N.I. (1995) Seismic anisotropy of shales. *Journal of Geophysical Research*, **100**, 5991−6003.

Jones, L.E.A. and Wang, H.F. (1981) Ultrasonic velocities in Cretaceous shales from the Williston Basin. *Geophysics*, **46**, 288−297.

Joswig, W., Fuess, H., Rothbauer, R., Takeuchi, Y., and Mason, S.A. (1980) A neutron diffraction study of a one-layer triclinic chlorite (penninite). *American Mineralogist*, **65**, 349−352.

Katahara, K.W. (1996) *Clay mineral elastic properties*. 66th SEG meeting, Denver, USA, expanded Abstracts, pp. 1691−1694.

Larson, A.C. and Von Dreele, R.B. (2004) *General Structure Analysis System (GSAS)*. Los Alamos National Laboratory Report LAUR 86−748.

Lonardelli, I., Wenk, H.-R., and Ren, Y. (2007) Preferred orientation and elastic anisotropy in shales. *Geophysics*, **72**, D33−D40.

Lutterotti, L., Matthies, S., and Wenk, H.-R. (1999) MAUD: a friendly Java program for materials analysis using diffraction. *International Union of Crystallography Committee Powder Diffraction Newsletter*, **21**, 14−15.

March, A. (1932) Mathematische Theorie der Regelung nach der Korngestalt bei affiner Deformation. *Zeitschrift für Kristallographie*, **81**, 285−297.

Matthies, S. and Humbert, M. (1993) The realization of the concept of a geometric mean for calculating physical constants of polycrystalline materials. *Physica Status Solidi*, **B177**, K47−K50.

Matthies, S. and Vinel, G.W. (1982) On the reproduction of the orientation distribution function of textured samples from reduced pole figures using the concept of conditional ghost correction. *Physica Status Solidi*, **B112**, K111−K114.

Mazurek, M., Hurford, A.J., and Leu, W. (2006) Unravelling the multi-stage burial history of the Swiss Molasse Basin: Integration of apatite fission track, vitrinite reflectance and biomarker isomerisation analysis. *Basin Research*, **18**, 27−50.

McCusker, L.B., Von Dreele, R.B., Cox, D.E., Louërd, D., and Scardi, P. (1999) Rietveld refinement guidelines. *Journal of Applied Crystallography*, **32**, 36−50.

Monecke, T., Koehler, S., Kleeberg, R., Herzig, P.M., and Gemmell, J.B. (2001) Quantitative phase analysis by the Rietveld method using X-ray powder diffraction data: Application to the study of alteration halos associated with volcanic-rock-hosted massive sulfide deposits. *The Canadian Mineralogist*, **39**, 1617−1633.

Moore, D.M. and Reynolds, R.C. (1997) *X-ray Diffraction and the Identification and Analysis of Clay Minerals*. Oxford University Press, New York, 378 pp.

Nagra (2002) *Projekt Opalinuston − Synthese der geowissenschaftlichen Untersuchungsergebnisse. Entsorgungsnachweis für abgebrannte Brennelemente, verglaste hochaktive sowie langlebige mittelaktive Abfälle.* Nagra Technical Report NTB 02-03, Nagra, Wettingen, Switzerland.

Oertel, G. (1983) The relationship of strain and preferred orientation of phyllosilicate grains in rocks − review. *Tectonophysics*, **100**, 413−447.

Oertel, G. and Curtis, C.D. (1972) Clay-ironstone concretion preserving fabrics due to progressive compaction. *Geological Society of America Bulletin*, **83**, 2597−2606.

Oertel, G. and Phakey, P.P. (1972) The texture of a slate from

Nantille, Caernarvon, North Wales. *Texture*, **1**, 1−8.

Omotoso, O. McCarty, D.K., Hillier, S., and Kleeberg, R. (2006) Some successful approaches to quantitative mineral analysis as revealed by the 3rd Reynolds Cup contest. *Clays and Clay Minerals*, **54**, 748−760.

Pearson, F. J., Arcos, D., Bath, A., Boisson, J.Y., Fernandez, A.M., Gäbler, H.E., Gaucher, E., Gautschi, A., Griffault, L., Hernan, P., and Waber, H.N. (2003) *Mont Terri project − Geochemistry of water in the Opalinus Clay formation at the Mont Terri Rock Laboratory*. Federal Office for Water and Geology Report 5, Bern, Switzerland.

Pellenard, P., Deconinck, J.F., Marchand, D., Thierry, J., Fortwengler, D., and Vigneron, G. (1999) Eustatic and volcanic influence during Middle Callovian Oxfordian clay sedimentation in the eastern part of the Paris Basin. *Compte rendus de l'Academie des Sciences*, **328**, 807−813.

Pellenard, P. and Deconinck, J.-F. (2006) Mineralogical variability of Callovo-Oxfordian clays from the Paris basin and the Subalpine Basin. *Comptes rendus Geoscience*, **338**, 854−866.

Ponte Castaneda, P. and Willis, J.R. (1995) The effect of spatial distribution on the effective behaviour of composite materials and cracked media. *Journal of the Mechanics and Physics of Solids*, **43**, 1919−1951.

Popa, N.C. (1998) The hkl dependence of diffraction-line broadening caused by strain and size for all Laue groups in Rietveld refinement. *Journal of Applied Crystallography*, **31**, 176−180.

Rebours, H., Armand, G., Cruchaudet, M., Dewonck, S., Morel, J., Righini, C., Vinsot, A., and Wileveau, Y. (2007) *Bilan 2006 des études et travaux menés par le laboratoire sur la formation du Callovo-Oxfordien*. Andra report DRPALS07-0496.

Rietveld, H.M. (1969) A profile refinement method for nuclear and magnetic structures. *Journal of Applied Crystallography*, **2**, 65−71

Sakharov, B.A., Lindgreen, H., Salyn, A., and Drits, V. (1999) Determination of illite-smectite structures using multispecimen XRD profile fitting. *Clays and Clays Minerals*, **47**, 555−566.

Sammartino, S., Bouchet, A., and Parneix, J.-C. (2001) *Construction d'un modèle conceptuel de la porosité et de la minéralogie dans les argilites du site de Bure*. Andra report DRP0ERM01-018.

Sammartino, S., Siitari-Kauppi, M., Meunier, A., Sardini, P., Bouchet, A., and Tevissen, E. (2002) An imaging method for the porosity of sedimentary rocks: Adjustment of the PMMA method - Example of a characterization of a calcareous shale. *Journal of Sedimentary Research*, **72**, 937−943.

Sammartino, S., Bouchet, A., Prêt, D., Parneix, J.-C., and Tevissen, E. (2003) Spatial distribution of porosity and minerals in clay rocks from the Callovo-Oxfordian formation (Meuse/Haute-Marne, Eastern France) − implications on ionic species diffusion and rock sorption capability. *Applied Clay Science*, **23**, 157−166.

Sato, H., Ono, K., Johnston, C.T., and Yamagishi, A. (2005) First-principles studies on elastic constants of a 1:1 layered kaolinite mineral. *American Mineralogist*, **90**, 1824−1826.

Sayers, C.M. (1994) The elastic anisotropy of shales. *Journal of Geophysical Research*, **99**, 767−774.

Sayers, C.M. (2005) Seismic anisotropy of shales. *Geophysical Prospecting*, **53**, 667−676.

Schoenberg, M. and Sayers, C.M. (1995) Seismic anisotropy of fractured rock. *Geophysics*, **60**, 204−211.

Sintubin, M. (1994a) Clay fabrics in relation to the burial history of shales. *Sedimentology*, **41**, 1161−1169.

Sintubin, M. (1994b) Phyllosilicate preferred orientation in relation to strain path determination in the lower Paleozoic

Stavelot-Venn Massif (Ardennes, Belgium). *Tectonophysics*, **237**, 215−231.

Solum, J.G., van der Pluijm, B.A., Peacor, D.R., and Warr, L.N. (2003) Mineralogy and microfabric of the Punchbowl Fault, an exhumed segment of the San Andreas Fault system. *Journal of Geophysical Research*, **108**, doi: 10.1029/2002JB001858

Solum, J.G., van der Pluijm, B.A., and Peacor, D.R. (2005) Neocrystallization, fabrics and age of clay minerals from an exposure of the Moab Fault, Utah. *Journal of Structural Geology*, **27**, 1563−1576.

Stixrude, L., and Peacor, D.R. (2002) First-principles study of illite-smectite and implications for clay mineral systems. *Nature*, **420**, 165−168.

Thomsen, L. (1986) Weak elastic anisotropy. *Geophysics*, **51**, 1954−1966.

Thomsen, L. (1995) Elastic anisotropy due to aligned cracks in porous rock. *Geophysical Prospecting*, **43**, 805−829.

Thury, M. and Bossart, P. (1999) The Mont Terri rock laboratory, a new international research project in a Mesozoic shale formation, in Switzerland. *Engineering Geology*, **52**, 347−359.

Trouiller, A. (2006) The Callovo-Oxfordian of the Paris Basin: From its geological context to the modelling of its properties. *Comptes rendus Geosciences*, **338**, 815−823.

Ufer, G., Roth, G., Kleeberg, R., Stanjek, H., Dohrmann, R., and Bergmann, J. (2004) Description of X-ray powder pattern of turbostratically disordered layer structures with a Rietveld compatible approach. *Zeitschrift für Kristallographie*, **219**, 519−527.

Valcke, S.L.A., Casey, M., Lloyd, G.E., Kendall, J.-M., and Fisher, Q.J. (2006) Lattice preferred orientation and seismic anisotropy in sedimentary rocks. *Geophysical Journal International*, **166**, 652−666.

Van Loon, L.R. and Soler, J.M. (2004) *Diffusion of HTO, $^{36}Cl^-$, $^{125}I^-$ and $^{22}Na^+$ in Opalinus Clay: Effect of confining pressure, sample orientation, sample depth and temperature*. PSI Report No. 04-03, Paul Scherrer Insitut, Villigen, Switzerland.

Van Loon, L.R., Soler, J.M., Müller, W., and Bradbury, M.H. (2004) Anisotropic diffusion in layered argillaceous rocks: a case study with Opalinus clay. *Environmental Science and Technology*, **38**, 5721−5728.

Vaughan, M.T. and Guggenheim, S. (1986) Elasticity of muscovite and its relationship to crystal structure. *Journal of Geophysical Research*, **91**, 4657−4664.

Vernik, L. and Liu, X. (1997) Velocity anisotropy in shales: A petrophysical study. *Geophysics*, **62**, 521−532.

Vernik, L. and Nur, A. (1992) Ultrasonic velocity and anisotropy of hydrocarbon source rocks. *Geophysics*, **57**, 727−735.

Viani, A., Gualtieri, A., and Artioli, G. (2002) The nature of disorder in montmorillonite by simulation of X-ray powder pattern. *American Mineralogist*, **87**, 966−975.

Wang, Z. (2002) Seismic anisotropy in sedimentary rocks, part 2: Laboratory data. *Geophysics*, **67**, 1423−1440.

Wenk, H.-R., Venkitasubramayan, C.S., Baker, D.W., and Turner, F.J. (1973) Preferred orientation in experimentally deformed limestone. *Contributions to Mineralogy and Petrology*, **38**, 81−114.

Wenk, H.-R., Matthies, S., Donovan, J., and Chateigner, D. (1998) BEARTEX, a Windows-based program system for quantitative texture analysis: *Journal of Applied Crystallography*, **31**, 262−269.

Wenk, H.-R., Lonardelli, I., Pehl, J., Devine, J., Prakapenka, V., Shen, G., and Mao, H.-K. (2004) In situ observation of texture development in olivine, ringwoodite, magnesiowuestite and silicate perovskite at high pressure. *Earth and Planetary Science Letters*, **226**, 507−519.

Wenk, H.-R., Lonardelli, I., Franz, H., Nihei, K., and Nakagawa, S. (2007) Preferred orientation and elastic anisotropy of illite-rich shale. *Geophysics*, **72**, E69−E75.

Yan, Y., van der Pluijm, B.A., and Peacor, D.R. (2001) Deformation microfabrics of clay gouge, Lewis Thrust, Canada: a case for fault weakening from clay transformation. Pp. 103−112 in: *The Nature and Tectonic Significance of Fault Zone Weakening* (R.E. Holdsworth, R.A. Strachan, J.F. Magloughlin, and R.J. Knipe, editors). Special Publication, **186**, Geological Society, London.

Young, R.A. (1993) *The Rietveld Method*. Oxford University Press, Oxford UK, 298 pp.

Yven, B., Sammartino, B., Géraud, Y., Homand, F., and Villiéras, F. (2006) Mineralogy, texture and porosity of Callovo-Oxfordian argillites of the Meuse/Haute-Marne region (eastern Paris Basin). Assemblage minéralogique, texture et porosité des argilites. *Mémoires de la Société géologique de France*, **178**, 73−90.